

1 **-Improving thermodynamic profile retrievals from microwave**  
2 **radiometers by including Radio Acoustic Sounding System (RASS)**  
3 **observations**

4  
5  
6 Irina V. Djalalova<sup>1,2</sup>, David D. Turner<sup>3</sup>, Laura Bianco<sup>1,2</sup>,  
7 James M. Wilczak<sup>2</sup>, James Duncan<sup>1,2,\*</sup>, Bianca Adler<sup>1,2</sup> and Daniel Gottas<sup>2</sup>

**Formatted:** Font color: Auto

8  
9 <sup>1</sup> Cooperative Institute for Research in Environmental Sciences (CIRES), Boulder, CO, USA

10 <sup>2</sup> National Oceanic and Atmospheric Administration, Physical Sciences Laboratory, Boulder, CO, USA

11 <sup>3</sup> ~~National~~ National Oceanic and Atmospheric Administration, Global Systems Laboratory, Boulder, CO USA

12  
13  
14  
15  
16  
17 ~~Draft: in preparation for Journal of Atmospheric Measurement Techniques (12/18/2020)~~

18 ~~-----~~ \*Now at WindESCo, Burlington, MA

19  
20  
21 **Formatted:** Space After: 12 pt, Line spacing: Double,  
Border: Top: (No border), Bottom: (No border), Left: (No  
border), Right: (No border), Between : (No border)

22

23

24

25 Corresponding author address: Irina V. Djalalova (Irina.V.Djalalova@noaa.gov), NOAA/Physical

26 Science Laboratory, 325 Broadway, mail stop: -PSD3, Boulder, CO 80305. Tel.: 303-497-6238.

27 Fax: 303-497-6181.

28

29 **Outline**

30 **Abstract**

31 **1. Introduction**

32 **2. XPIA dataset**

33 **2.1 MWR measurements**

34 **2.2 Radiosonde measurements**

35 **2.3 WPR-RASS measurements**

36 **2.4 BAO data**

37 **3. Physical retrievals**

38 **3.1 Iterative retrieval technique**

39 **3.2 ~~PR's~~Physical retrieval bias correction and temperature profiles**

40 **3.3 Averaging kernel**

41 **4. Results**

42 **4.1 ~~PR's~~Physical retrieval statistical analysis from Akernel**

43 **4.2 Statistical analysis of ~~PRs compared to NN~~physical retrievals up to 5 km AGL**

**Formatted:** Outline numbered + Level: 1 + Numbering Style: 1, 2, 3, ... + Start at: 1 + Alignment: Left + Aligned at: 0" + Indent at: 0.25"

**Formatted:** Outline numbered + Level: 1 + Numbering Style: 1, 2, 3, ... + Start at: 1 + Alignment: Left + Aligned at: 0" + Indent at: 0.25"

**Formatted:** Outline numbered + Level: 2 + Numbering Style: 1, 2, 3, ... + Start at: 1 + Alignment: Left + Aligned at: 0.25" + Indent at: 0.5"

**Formatted:** Outline numbered + Level: 1 + Numbering Style: 1, 2, 3, ... + Start at: 1 + Alignment: Left + Aligned at: 0" + Indent at: 0.25"

**Formatted:** Space After: 12 pt, Line spacing: Double, Border: Top: (No border), Bottom: (No border), Left: (No border), Right: (No border), Between : (No border)

44 **4.3 Statistics for the least close to the climatological profiles**

45 **4.4 Virtual temperature statistics**

46 **5. Conclusions**

47 **Appendix A**

48 **Data availability**

49 **Author contribution**

50 **Acknowledgments**

51 **References**

52

53 **Abstract**

54 Thermodynamic profiles are often retrieved from the multi-wavelength brightness  
55 temperature observations made by microwave radiometers (MWRs) using regression methods  
56 (linear, quadratic approaches), artificial intelligence (neural networks), or physical-iterative  
57 methods. Regression and neural network methods are tuned to mean conditions derived from  
58 a climatological dataset of thermodynamic profiles collected nearby. In contrast, physical-  
59 iterative retrievals use a radiative transfer model starting from a climatologically reasonable  
60 value of temperature and water vapor, with the model run iteratively until the derived  
61 brightness temperatures match those observed by the MWR within a specified uncertainty.

62 In this study, a physical-iterative approach is used to retrieve temperature and humidity  
63 profiles from data collected during XPIA (eXperimental Planetary boundary layer Instrument  
64 Assessment), a field campaign held from March to May 2015 at NOAA's Boulder Atmospheric  
65 Observatory (BAO) facility. During the campaign, several passive and active remote sensing

**Formatted:** Outline numbered + Level: 1 + Numbering  
Style: 1, 2, 3, ... + Start at: 1 + Alignment: Left + Aligned  
at: 0" + Indent at: 0.25"

**Formatted:** Space After: 12 pt, Line spacing: Double,  
Border: Top: (No border), Bottom: (No border), Left: (No  
border), Right: (No border), Between : (No border)

66 instruments as well as in-situ platforms were deployed and evaluated to determine their  
67 suitability for the verification and validation of meteorological processes. Among the deployed  
68 remote sensing instruments was a multi-channel MWR, as well as two radio acoustic sounding  
69 systems (RASS), associated with 915-MHz and 449-MHz wind profiling radars.

70 Having the possibility to combine the information provided by the MWR and RASS  
71 systems, in this study the physical-iterative approach is tested with different observational  
72 inputs: first using data from surface sensors and the MWR in different configurations, and then  
73 including data from the RASS. These temperature retrievals are ~~also compared to those derived~~  
74 ~~by a neural network method, assessing their relative accuracy~~ assessed against 58 co-located  
75 radiosonde profiles. Results show that the combination of the MWR and RASS observations in  
76 the physical-iterative approach allows for a more accurate characterization of low-level  
77 temperature inversions, and that these retrieved temperature profiles match the radiosonde  
78 observations better than ~~all other approaches, including the neural network temperature~~  
79 ~~profiles retrieved from only the MWR~~, in the ~~atmospheric~~ layer between the surface and 5 km  
80 ~~above ground level (AGL-)~~. Specifically, in this layer of the atmosphere, both root mean square  
81 errors and standard deviations of the difference between radiosonde and retrievals that  
82 combine MWR and RASS are improved by  $\sim 0.5$  °C compared to the other methods. Pearson  
83 correlation coefficients are also improved.

**Formatted:** Font: Calibri, 12 pt, Font color: Auto, Not Highlight

**Formatted:** Space After: 12 pt, Line spacing: Double, Border: Top: (No border), Bottom: (No border), Left: (No border), Right: (No border), Between : (No border)

87 We provide the comparison of the temperature physical retrievals to the neural network  
88 retrievals in Appendix A.

89  
90  
91  
92  
93  
94  
95  
96  
97  
98  
99

100 **1. Introduction**

101 To monitor the state of the atmosphere for process understanding and for model  
102 verification and validation, scientists rely on observations from a variety of instruments, each  
103 one having its set of advantages and disadvantages. Using several diverse instruments allows  
104 one to monitor different aspects of the atmosphere, while combining them in an optimized  
105 synergetic approach can improve the accuracy of the information we have on the state of the  
106 atmosphere.

107 During the eXperimental Planetary boundary layer Instrumentation Assessment (XPIA)  
108 campaign, an U.S. Department of Energy sponsored experiment held at the Boulder

**Formatted:** Outline numbered + Level: 1 + Numbering  
Style: 1, 2, 3, ... + Start at: 1 + Alignment: Left + Aligned  
at: 0.25" + Indent at: 0.5"

**Formatted:** Space After: 12 pt, Line spacing: Double,  
Border: Top: (No border), Bottom: (No border), Left: (No  
border), Right: (No border), Between : (No border)

109 Atmospheric Observatory (BAO) in Spring 2015, several instruments were deployed (Lundquist  
110 et al., 2017) with the goal of assessing their capability for measuring flow within the  
111 atmospheric boundary layer. XPIA investigated novel measurement approaches, and quantified  
112 uncertainties associated with these measurement methods. While the main interest of the XPIA  
113 campaign was on wind and turbulence, measurements of other important atmospheric  
114 variables were also collected, including temperature and humidity. Among the deployed  
115 instruments were two identical microwave radiometers (MWRs) and two radio acoustic  
116 sounding systems (RASS), as well as radiosondes launches that were used for verification.

117 MWRs are passive sensors, sensitive to atmospheric temperature and humidity content  
118 that allow for a high temporal observation of the state of the atmosphere, with some  
119 advantages and limitations. In order to estimate profiles of temperature and humidity, ~~they~~  
120 ~~observe atmospheric from the observed~~ brightness ~~temperature and apply radiative transfer~~  
121 ~~equations (Rosenkranz, 1998) and~~ temperatures ( $T_b$ ), several methods could be applied such as  
122 ~~regressions~~, neural network retrievals ~~(Solheim et al., 1998a, and 1998b; Ware et al., 2003)~~, or  
123 physical retrieval methodologies ~~that can~~ which include more information about the  
124 atmospheric state in the retrieval process ~~(Turner and Blumberg, 2019)~~. ~~Radiative transfer~~  
125 ~~equations (Rosenkranz, 1998) are commonly used to train statistical retrievals, or as forward~~  
126 ~~models used within physical retrieval methods~~. Advantages of MWRs include their compact  
127 design, the relatively high temporal resolution of the measurements (2-3 minutes), the  
128 possibility to observe the vertical structure of both temperature and moisture, ~~through~~ the  
129 ~~deep layer~~ depth of the ~~atmosphere that can be monitored including~~ troposphere during ~~both~~  
130 ~~clear and~~ cloudy conditions, and their capability to operate in a standalone mode.

131 Disadvantages include ~~the~~ limited accuracy, ~~as the temperature and humidity profiles are not~~  
132 ~~actively measured but retrieved, their lower accuracy~~ in the presence of rain because of  
133 scattering of radiation ~~due to~~from raindrops in the atmosphere (and because ~~some~~ water can  
134 ~~still~~ deposit on the radome, although the instruments use a hydrophobic radome and force  
135 airflow over the surface of the radome during rain to mitigate this impact), rather coarse  
136 vertical resolution, and for retrievals the necessity to have a site-specific climatology. Other  
137 disadvantages include the challenges related to performing accurate calibrations (Küchler et al.,  
138 2016, and references within), radio frequency interference (RFI), and the low accuracy on the  
139 retrieved liquid water path (LWP) especially for values of LWP less than ~~50~~20 g/m<sup>2</sup>.

140 RASS, in comparison, are active instruments that emit a longitudinal acoustic wave  
141 upward, causing a local compression and rarefaction of the ambient air. These density  
142 variations are tracked by the Doppler radar associated with the RASS, and the speed of the  
143 propagating sound wave is measured. The speed of sound is related to the virtual temperature  
144 ( $T_v$ ) (North et al., 1973), and therefore, RASS are routinely used to remotely measure vertical  
145 profiles of virtual temperature in the boundary layer. Being an active instrument, the RASS is in  
146 general more accurate than a passive instrument (Bianco et al., 2017), but they also come with  
147 their sets of disadvantages. The main limitations of RASS for retrieval purposes are its low  
148 temporal resolution (typically a 5-min averaged RASS profile is measured once or twice per  
149 hour), and their limited altitude coverage. Recent studies (Adachi and Hashiguchi, 2019) have  
150 shown that to make them more suitable to operate in urban areas RASS could use parametric  
151 speakers to take advantage of their high directivity and very low side lobes. Nevertheless, the  
152 maximum height reached by the RASS is still limited, being a function of both radar frequency

153 and atmospheric conditions (May and Wilczak, 1993), and is determined both by the  
154 attenuation of the sound, which is a function of atmospheric temperature, humidity, and  
155 frequency of the sound source, and the advection of the propagating sound wave out of the  
156 radar's field-of-view. Therefore, data availability is usually limited to the lowest several ~~km,~~  
157 ~~dependent~~kilometers, depending on the frequency of the radar. In addition, wintertime  
158 coverage is usually considerably lower than that in summer, due to a higher probability of  
159 stronger winds advecting the sound wave away from the radar in the winter.

160 To get a better picture of the state of the temperature and moisture structure of the  
161 atmosphere, it makes sense to try to combine the information obtained by both MWR and  
162 RASS. Integration of different instruments has been of scientific interest for several years (Han  
163 and Westwater 1995; Stankov et al. 1996; Bianco et al., 2005; Engelbart et al., 2009; Cimini et  
164 al., 2020;~~;~~ Turner and Löhnert, 2020, to name some). In this study we particularly focus on the  
165 combination of the MWR and RASS observations in the retrievals to improve the accuracy of  
166 the temperature profiles in the lowest 5 km compared to ~~the standard MWR retrievals~~  
167 ~~obtained through neural network (NN) processing, or compared to~~ physical retrieval  
168 approaches that do not include the information from RASS measurements. Some studies have  
169 used analyses from numerical weather prediction (NWP) models as an additional constraint in  
170 these variational retrievals (e.g., Hewison 2007; Cimini et al. 2005, 2011; Martinet et al. 2020);  
171 however, we have elected not to include model data in this study because we wanted to  
172 evaluate the impact of the RASS profiles on the retrievals from a purely observational  
173 perspective.



174 This paper is organized as follows: Section 2 summarizes the experimental dataset;  
175 Section 3 introduces the principles of the physical retrieval approaches used to obtain vertical  
176 profiles of the desired variables; Section 4 produces statistical analysis of the comparison  
177 between the different retrieval approaches and radiosonde measurement; finally, conclusions  
178 are presented in Section 5.

179

## 180 2. XPIA data

181 The data used in our analysis were collected during the XPIA experiment, held in Spring  
182 2015 (March-May) at the NOAA's Boulder Atmospheric Observatory (BAO) site, in Erie,  
183 Colorado (Lat.: 40.0451 N, Lon.: 105.0057 W, El.: 1584 m MSL). XPIA was the last experiment  
184 conducted at this facility, as after almost 40 years of operations the BAO 300-m tower was  
185 demolished at the end of 2016 (Wolfe and Lataitis, 2018). XPIA was designed to assess the  
186 capability of different remote sensing instruments for quantifying boundary layer structure, and  
187 was a preliminary study as many of these same instruments were later deployed, among other  
188 campaigns, for the second Wind Forecast Improvement Project WFIP2 (Shaw et al., 2019;  
189 Wilczak et al., 2019) which investigated flows in complex terrain for wind energy applications,  
190 and were for example used to study cold air pool and gap flow characteristics (Adler et al.,  
191 ~~2020~~2021; Banta et al., 2020; Neiman et al., 2019). The list of the deployed instruments  
192 included active and passive remote-sensing devices, and in-situ instruments mounted on the  
193 BAO tower. Data collected during XPIA are publicly available at  
194 <https://a2e.energy.gov/projects/xpia>. A detailed description of the XPIA experiment can be

**Formatted:** Outline numbered + Level: 1 + Numbering  
Style: 1, 2, 3, ... + Start at: 1 + Alignment: Left + Aligned  
at: 0.25" + Indent at: 0.5"

**Formatted:** Space After: 12 pt, Line spacing: Double,  
Border: Top: (No border), Bottom: (No border), Left: (No  
border), Right: (No border), Between : (No border)

195 found in Lundquist et al. (2017), while a specific look at the accuracy of the instruments used in  
196 this study can be found in Bianco et al. (2017).

197

## 198 2.1 MWR measurements

199 Two identical MWRs, (Radiometrics MP-3000A), managed by NOAA (MWR-NOAA) and by

**Formatted:** Font: 11 pt, Highlight

200 the University of Colorado (MWR-CU), were deployed next to each other at the visitor center

201 ~600 m south of the BAO tower (see Lundquist et al., 2017 for a detailed map of the study

202 area). Prior to the experiment, both MWRs were calibrated using an external liquid nitrogen

203 target and an internal ambient target and thoroughly serviced (sensor cleaning, radome

204 replacement, etc.). MWRs are passive devices which record the natural microwave emission in

205 the water vapor and oxygen absorption bands from the atmosphere, providing measurements

206 of the brightness temperatures. Both MWRs have 35-channels spanning a range of frequencies,

207 with 21 channels in the lower (22-30 GHz) K-band frequency band, of which 8 channels were

208 used during XPIA: 22.234, 22.5, 23.034, 23.834, 25, 26.234, 28 and 30 GHz; and 14 channels in

209 the higher (51-59 GHz) V-band frequency band, of which all were used in XPIA: 51.248, 51.76,

210 52.28, 52.804, 53.336, 53.848, 54.4, 54.94, 55.5, 56.02, 56.66, 57.288, 57.964 and 58.8 GHz.

211 Frequencies in the K-band are more sensitive to water vapor and cloud liquid water, while

212 frequencies in the V-band are sensitive to atmospheric temperature due to the absorption of

213 atmospheric oxygen (Cadeddu et al., 2013). V-band frequencies or channels also can be divided

214 in two categories: the opaque channels, 56.66 GHz and higher, that are more informative in the

215 layer of the atmosphere from the surface to ~1 km AGL, and the transparent channels, 51-56

216 GHz, that are more informative above 1 km AGL. Both MWRs observed at the zenith and at 15-

**Formatted:** Space After: 12 pt, Line spacing: Double,  
Border: Top: (No border), Bottom: (No border), Left: (No  
border), Right: (No border), Between : (No border)

217 and 165-degree elevation angles in the north-south plane (referred to as oblique elevation  
218 scans hereafter; note zenith views have 90-degree elevation ~~angles~~angle). In addition, each  
219 MWR was provided with a separate surface sensor to measure pressure, temperature, and  
220 relative humidity at the installation level that was ~2.5 m ~~above ground level (AGL)~~AGL. ~~MWRs~~  
221 ~~are passive devices which record the natural microwave emission in the water vapor and~~  
222 ~~oxygen absorption bands from the atmosphere, providing measurements of the brightness~~  
223 ~~temperatures.~~ Vertical profiles of temperature (T), water vapor density (WVD), and relative  
224 humidity (RH) were retrieved in real-time during XPIA every 2-3 minutes using a neural network  
225 (NN) approach provided by the manufacturer of the radiometer, Radiometrics (Solheim et al.  
226 1998a, and 1998b; Ware et al., 2003 ~~NN approach provided by the private manufacturing~~  
227 ~~company Radiometrics (Solheim et al. 1998). The NN used a training dataset based on a 5-year~~  
228 ~~climatology of profiles from radiosondes launched at the Denver International Airport, 35 miles~~  
229 ~~south east from the XPIA site. NN-based MWR vertical retrieval profiles were obtained using~~  
230 ~~the zenith and an average of two oblique elevation scans, all extending for 58 levels up to 10~~  
231 ~~km, with nominal vertical levels depending on the height (every 50 m from the surface to 500~~  
232 ~~m, every 100 m from 500 m to 2 km, and every 250 m from 2 to 10 km, AGL). In this study we~~  
233 ~~make use of the NN zenith and of the NN oblique, where the latter can average out small-scale~~  
234 ~~horizontal inhomogeneities of the atmosphere).~~ Although the physical retrieval configurations  
235 used in this study do not exactly match the MWR configurations used for NN retrievals, a  
236 comparison of both physical and neural network retrievals to the radiosonde temperature data  
237 is presented in Appendix A.

238 ~~The MWR-CU~~ Both MWRs nominally operated from 9 March to 7 May 2015,  
239 ~~while~~ although the MWR-NOAA was unavailable between 5-27 April 2015. For the overlapping  
240 dates, temperature profiles retrieved from the two MWRs showed very good agreement with  
241 less than 0.5 ~~K~~<sup>°C</sup> bias and 0.994 correlation (Bianco et al., 2017). For this reason, and because  
242 the MWR-CU was available for a longer time period, we use only the MWR-CU (hereafter simply  
243 called MWR).

244

## 245 2.2 Radiosonde measurements

246 Between 9 March and 7 May 2015, while the MWR was operational, radiosondes were  
247 launched by the National Center for Atmospheric Research (NCAR) assisted by several students  
248 from the University of Colorado over three selected periods, one each in March, April, and May.  
249 There was a total of 59 launches, mostly four times per day, around 14:00, 18:00, 22:00 and  
250 0200 UTC (8:00, 12:00, 16:00 and 20:00 local standard time, LST). All radiosondes were Vaisala  
251 RS92. The first 35 launches, between 9-19 March, were done from the visitor center, while the  
252 11 launches, between 15-22 April, and 13 launches, between 1-4 May, were done from the  
253 water tank site, ~1000 meters apart (see Lundquist et al., 2017 for a detailed map of the study  
254 area). The radiosonde measurements included temperature, dewpoint temperature, and  
255 relative humidity, to altitudes usually higher than 10 km AGL, with measurements every few  
256 seconds.

257

## 258 2.3 WPR-RASS measurements

Formatted: Indent: First line: 0.5"

Formatted: Font: Not Bold

Formatted: Indent: First line: 0.5"

Formatted: Space After: 12 pt, Line spacing: Double,  
Border: Top: (No border), Bottom: (No border), Left: (No  
border), Right: (No border), Between : (No border)

259 Two NOAA wind profiling radars (WPRs), operating at frequencies of 915-MHz and 449-  
260 MHz, were deployed at the visitor center (same location ~~of~~as the MWR) during XPIA. These  
261 systems are primarily designed to measure the vertical profile of the horizontal wind vector, but  
262 co-located RASS also observe profiles of virtual temperature in the lower atmosphere, with  
263 different resolutions and height coverages depending on the WPR. Thus, the RASS associated  
264 with the 915-MHz WPR (hereafter referred to as RASS 915) measured virtual temperature from  
265 120 to 1618 m with a vertical resolution of 62 m, and the 449 MHz RASS (hereafter referred to  
266 as RASS 449) sampled the boundary layer from 217 to 2001 m with a vertical resolution of 105  
267 m. The maximum height reached by the RASS is a function of both radar frequency and  
268 atmospheric conditions (May and Wilczak, 1993), and is usually lower for RASS 915 data, as will  
269 be shown later in the analysis.

270 The RASS data were processed using a radio frequency interference (RFI)-removal  
271 algorithm (performed on the RASS spectra), a consensus algorithm (Strauch et al. 1984)  
272 performed on the moment data using a 60% consensus threshold, a Weber-Wuertz outlier  
273 removal algorithm (Weber et al., 1993) performed on the consensus averages, and a RASS  
274 range-correction algorithm (Görsdorf and Lehmann, 2000) using an average relative humidity  
275 setting of 50% determined from the available observations.

276

#### 277 **2.4 BAO data**

278 The BAO 300-m tower was built in 1977 to study the planetary boundary layer (Kaimal  
279 and Gaynor 1983). During XPIA, measurements were collected at the surface (2 m) and at six  
280 higher levels (50, 100, 150, 200, 250 and 300 m AGL). -Each tower level was equipped with 2

281 sonic anemometers on orthogonal booms, and one sensor based on a Sensiron SHT75 solid-  
282 state sensor to measure temperature and relative humidity with a time resolution of 1 s, and  
283 averaged over five minutes.

284 The observational temperature and water vapor surface data are used from the more  
285 accurate observations at the BAO tower 2 m AGL level (Horst, [et al.](#), 2016), to replace the data  
286 measured by the less accurate MWR inline surface sensor.

287  
288

### 289 3. Physical retrievals

290 ~~Other than NN approaches, a~~ physical retrieval (PR) iterative approach can be used to  
291 retrieve vertical profiles of thermodynamic properties from the MWR observations (Maahn et  
292 al 2020). In this case, using a radiative transfer model, the process starts with a climatologically  
293 reasonable value of temperature and water vapor, and is iteratively repeated until the  
294 computed brightness temperatures match those observed by the MWR within the uncertainty  
295 of the observed brightness temperatures (Rodgers, 2000; Turner and Löhnert, 2014; Maahn et  
296 al. 2020).

297  
298

#### 298 3.1 Iterative retrieval technique

299 For this study, the ~~physical retrieval (PR)~~PR uses a microwave radiative transfer model,  
300 MonoRTM (Clough et al., 2005), which is fully functional for the microwave region and was  
301 intensively evaluated previously on MWR measurements (Payne et al. 2008; 2011). We start  
302 with the state vector  $\mathbf{X}_a = [\mathbf{T}, \mathbf{Q}, \text{LWP}]^T$ , where superscript T denotes transpose.  $\mathbf{T}$  (K) and  $\mathbf{Q}$

**Formatted:** Outline numbered + Level: 1 + Numbering Style: 1, 2, 3, ... + Start at: 1 + Alignment: Left + Aligned at: 0.25" + Indent at: 0.5"

**Formatted:** Space Before: 0 pt, After: 0 pt

**Formatted:** Space Before: 0 pt, After: 0 pt, Border: Top: (No border), Bottom: (No border), Left: (No border), Right: (No border), Between : (No border)

**Formatted:** Space After: 12 pt, Line spacing: Double, Border: Top: (No border), Bottom: (No border), Left: (No border), Right: (No border), Between : (No border)

303 (g/kg) are temperature and water vapor mixing ratio profiles at 55 vertical levels from the  
 304 surface up to 17 km, with the distance between the levels increasing exponentially-like with  
 305 height. LWP is the liquid water path in (g/m<sup>2</sup>) that measures the integrated content of liquid  
 306 water in the entire vertical column above the MWR, and is a scalar. For this study we have  $X_a$   
 307 with dimensions equal to 111 x 1 (two vectors  $T$  and  $Q$  with 55 levels each, and LWP). -We are  
 308 using the retrieval framework of Turner and Blumberg (2019), but only using MWR data (no  
 309 spectral infrared) and will augment the retrieval to include RASS profiles of  $T_v$ .

310 \_\_\_\_\_ The observation vector  $Y$  from the beginning includes temperature and water vapor  
 311 mixing ratio measured at the surface, and brightness temperature ( $T_b$ ) measured by the MWR.  
 312 The MonoRTM model  $F$  is used as the forward model to estimate the observation vector  $Y$  from  
 313 the current state vector  $X$ , from Eq. (1), and is then compared to the observation vector  $Y$ ,  
 314 iterating until the difference between  $F(X)$  and  $Y$  is small within a specified uncertainty:.

Formatted: Indent: First line: 0"

Formatted: Font: 11 pt

Formatted: Font: Not Bold

315 ~~$$X_{n+1} = X_n + (S_a^{-1} + K^T S_\epsilon^{-1} K)^{-1} K^T S_\epsilon^{-1} [Y - F(X_n) + K(X_n - X_a)] \quad (1)$$~~

$$X_{n+1} = X_n + (S_a^{-1} + K^T S_\epsilon^{-1} K)^{-1} K^T S_\epsilon^{-1} [Y - F(X_n) + K(X_n - X_a)] \quad (1)$$

317 with: \_\_\_\_\_

318 
$$X_a = \begin{bmatrix} T \\ Q \\ L \end{bmatrix} \quad S_a = \begin{bmatrix} \sigma_{TT}^2 & \sigma_{TQ}^2 & 0 \\ \sigma_{QT}^2 & \sigma_{QQ}^2 & 0 \\ 0 & 0 & \sigma_L^2 \end{bmatrix} \quad K_{ij} = \frac{\partial F_i}{\partial X_j}$$

319 
$$S_\epsilon = \begin{bmatrix} \sigma_{T_{sfc}}^2 & 0 & 0 & 0 & 0 \\ 0 & \sigma_{Q_{sfc}}^2 & \textcircled{1} & 0 & 0 \\ 0 & 0 & \sigma_{T_b_{zenith}}^2 & 0 & \textcircled{2} \\ 0 & 0 & 0 & \sigma_{T_b_{zenith+oblique}}^2 & 0 \\ 0 & 0 & 0 & 0 & \sigma_{T_{vRASS915(449)}}^2 \end{bmatrix}$$

Formatted: Space After: 12 pt, Line spacing: Double, Border: Top: (No border), Bottom: (No border), Left: (No border), Right: (No border), Between : (No border)

$$\begin{aligned}
 \mathbf{X}_a &= \begin{bmatrix} T \\ Q \\ LWP \end{bmatrix} & \mathbf{S}_a &= \begin{bmatrix} \sigma_{TT}^2 & \sigma_{TQ}^2 & 0 \\ \sigma_{QT}^2 & \sigma_{QQ}^2 & 0 \\ 0 & 0 & \sigma_{LWP}^2 \end{bmatrix} & K_{ij} &= \frac{\partial F_i}{\partial X_j} \\
 \mathbf{S}_\varepsilon &= \begin{bmatrix} \sigma_{T_{sfc}}^2 & 0 & 0 & 0 \\ 0 & \sigma_{Q_{sfc}}^2 & 0 & 0 \\ 0 & 0 & \sigma_{Tb_{zenith}}^2 \textcircled{1} & \text{or } \sigma_{Tb_{zenith+oblique\ avrg}}^2 \textcircled{2} \\ 0 & 0 & 0 & \sigma_{Tv_{RASS915(449)}}^2 \textcircled{3\ or\ 4} \end{bmatrix}
 \end{aligned}$$

326 where  $i$  and  $j$  in the  $K_{ij}$  definition mark channel and vertical level respectively, and  $\mathbf{Y}$ , depending

Formatted: Indent: First line: 0"

327 on the configuration used, being equal to:

$$\mathbf{Y}_1 = \begin{bmatrix} T_{sfc} \\ Q_{sfc} \\ Tb_{zenith} \end{bmatrix} \quad \mathbf{Y}_2 = \begin{bmatrix} T_{sfc} \\ Q_{sfc} \\ Tb_{zenith} \\ Tb_{zenith+oblique} \end{bmatrix}$$

$$\mathbf{Y}_3 = \begin{bmatrix} T_{sfc} \\ Q_{sfc} \\ Tb_{zenith} \\ Tb_{zenith+oblique} \\ Tv_{RASS915} \end{bmatrix} \quad \mathbf{Y}_4 = \begin{bmatrix} T_{sfc} \\ Q_{sfc} \\ Tb_{zenith} \\ Tb_{zenith+oblique} \\ Tv_{RASS449} \end{bmatrix}$$

$$\mathbf{Y}_1 = \begin{bmatrix} T_{sfc} \\ Q_{sfc} \\ Tb_{zenith} \end{bmatrix} \quad \mathbf{Y}_2 = \begin{bmatrix} T_{sfc} \\ Q_{sfc} \\ Tb_{zenith+oblique\ avrg} \end{bmatrix}$$

$$\mathbf{Y}_3 = \begin{bmatrix} T_{sfc} \\ Q_{sfc} \\ Tb_{zenith+oblique\ avrg} \\ Tv_{RASS915} \end{bmatrix} \quad \mathbf{Y}_4 = \begin{bmatrix} T_{sfc} \\ Q_{sfc} \\ Tb_{zenith+oblique\ avrg} \\ Tv_{RASS449} \end{bmatrix}$$

Formatted: Space After: 12 pt, Line spacing: Double, Border: Top: (No border), Bottom: (No border), Left: (No border), Right: (No border), Between : (No border)



336 The superscripts T and -1 in (1) indicate transpose or inverse matrix, respectively. Also,  
337 vectors and matrices are shown in bold.- Note that we are including the 2-m surface-level  
338 observations of temperature and water vapor mixing ratio (Tsfc and Qsfc, respectively) as part  
339 of the observation vector **Y**, and thus the uncertainties in these observations are included in **S<sub>ε</sub>**.

**Formatted: Font: Bold**

340 The first guess of the state vector **X**, **X<sub>1</sub>** in Eq. (1), is set to be equal to the mean state  
341 vector of climatological estimates, or a “prior” vector **X<sub>a</sub>**, which is calculated independently for  
342 each month of the year from climatological sounding profiles (using 10 years of data) in the  
343 Denver area.

344 **S<sub>a</sub>** is the covariance matrix of the “prior” vector that includes not only temperature or  
345 water vapor variances but also the covariances between them. Using 3,000 radiosondes  
346 launched by the NWS in Denver, we interpolated each radiosonde profile to the vertical levels  
347 used in the retrieval, after which we computed the covariance of temperature and  
348 temperature, temperature and humidity, and humidity and humidity for different levels. **K** is  
349 the Jacobian matrix, computed using finite differences by perturbing the elements of **X** and  
350 rerunning the radiative transfer model.

**Formatted: Indent: First line: 0.5"**

**Formatted: Font: Bold**

351 We start with four configurations for the observational vector **Y** (**Y<sub>1</sub>**, **Y<sub>2</sub>**, **Y<sub>3</sub>**, and **Y<sub>4</sub>**). The  
352 MWR provides the **T<sub>b</sub>** measurements in all schemes, from 22 channels from the zenith scan for  
353 the zenith only in configuration (**Y<sub>1</sub>**), which also includes the 2-m in-situ observations of  
354 temperature and humidity), and while when using the zenith and plus oblique in **T<sub>b</sub>** inputs (**Y<sub>2</sub>**,  
355 **Y<sub>3</sub>**, and **Y<sub>4</sub>**, also including the 2-m in-situ observations of temperature and humidity) the same  
356 22 channels were used from the zenith scans together with only the four opaque channels  
357 (56.66, 57.288, 57.964 and 58.8 GHz) from the oblique scans. Using additional measurements

**Formatted: Font: Bold**

**Formatted: Space After: 12 pt, Line spacing: Double, Border: Top: (No border), Bottom: (No border), Left: (No border), Right: (No border), Between : (No border)**

358 from the co-located radar systems with RASS, we may further expand the observational vector  
 359 with either RASS 915 ( $Y_3$ ) or RASS 449 ( $Y_4$ ) virtual temperature observations. The covariance  
 360 matrix of the observed data,  $S_e$ , depends on the chosen  $Y_i$  as it is highlighted by the red  
 361 numbers in the matrix description, with increasing dimensions from  $Y_1$  to  $Y_2$  and additional  
 362 increasing dimensions to  $Y_3$  and/or  $Y_4$  through the multi-level measurements of the RASS (Turner  
 363 and Blumberg, 2019). Table 1 summarizes the observational information included in these four  
 364 different configurations of the PR.

365

	$T_{sfc}$	$Q_{sfc}$	$Tb_{zenith}$	<del><math>Tb_{zenith}</math></del> <i>oblique <math>Tb_{oblique}</math></i> <del><math>avg</math></del>	$TV_{RASS915}$	$TV_{RASS449}$
$Y_1 = MWRz$	X	X	X			
$Y_2 = MWRzO$	X	X	X	X		
$Y_3 = MWRzO915$	X	X	X	X	X	
$Y_4 = MWRzO449$	X	X	X	X		X

366 Table 1. Four PR configurations corresponding to the four observational  $Y_i$  vectors in Eq. (1).

367

368 The uncertainty in the MWR  $Tb$  observations was set to the standard deviation from a  
 369 detrended time-series analysis for each channel during cloud-free periods, which is described in  
 370 detail in Section 3.2. The derived uncertainties ranged from 0.3 K to 0.4 K in the 22 to 30 GHz

- Formatted: Font: 14 pt, Italic
- Formatted: Space After: 8 pt, Line spacing: Multiple 1.08 li
- Formatted: Font: 11 pt, Italic
- Formatted: Indent: First line: 0", Space After: 8 pt, Line spacing: Multiple 1.08 li
- Formatted Table
- Formatted: Font: 14 pt, Italic
- Formatted: Font: 14 pt, Italic
- Formatted: Space After: 8 pt, Line spacing: Multiple 1.08 li
- Formatted: Font: 14 pt, Italic
- Formatted: Space After: 8 pt, Line spacing: Multiple 1.08 li
- Formatted: Font: 14 pt, Italic
- Formatted: Space After: 8 pt, Line spacing: Multiple 1.08 li
- Formatted: Space After: 12 pt, Line spacing: Double, Border: Top: (No border), Bottom: (No border), Left: (No border), Right: (No border), Between : (No border)

371 channels, and 0.4 to 0.7 K in the 52 to 60 GHz channels. We ~~assume~~assumed that there ~~is~~was  
372 no ~~covariance~~correlated error between the different ~~instruments~~MWR channels.

373 For the RASS, collocated RASS and radiosonde profiles were compared and the standard  
374 deviation of the differences in  $T_v$  were determined as well as a function of the radar's signal-to-  
375 noise ratio (SNR). This relationship resulted in uncertainties that ranged from 0.8 K at high SNR  
376 values to 1.5 K at low SNR values. Again, we assumed that there was no correlated error  
377 between different channels (MWR) or height levels (RASS) of each instrument, therefore  
378 this RASS heights. Following all these assumptions, the covariance matrix  $S_e$  is diagonal.

379 The Jacobian matrix,  $K$ , has dimensions  $m \times 111$ , where  $m$  is the length of the vector  $Y_i$ ,  
380 therefore its ~~dimensions increased~~dimension increases correspondingly with the inclusion of  
381 more observational data.  $K$  makes the “connection” between the state vector and the  
382 observational data and should be calculated at every iteration.

### 384 **3.2 ~~Bias~~Physical retrieval bias-correction and temperature profiles**

385 Observational errors propagate through the retrieval into the derived profiles (i.e. the  
386 bias of the observed data will contribute to a bias in the retrievals.) For that, retrieval  
387 uncertainties in Eq. (1) from  $Y = Y_1$  or  $Y_2$  derive only from uncertainties in surface and MWR  
388 data, while retrieval uncertainties from  $Y = Y_3$  or  $Y_4$  are coming from uncertainties in surface,  
389 MWR, and RASS measurements.

390 While the bias of the retrieval depends on both the sensitivity of the forward model and  
391 the observational ~~uncertainty~~systematic offset, we can try to eliminate, or at least to reduce,  
392 the systematic error in the MWR observations. To this aim, we first looked for clear sky days (to

393 reduce the degrees of freedom associated with clouds) during the period of the measurements.

394 One method to identify clear-sky times is to use ~~brightness temperature-Tb~~ observations in the  
395 30 GHz liquid water ~~vapor~~-sensitive channel. The random uncertainty in ~~brightness temperature~~  
396 ~~was-Tb is~~ calculated as ~~its~~an average of the Tb standard deviation ~~during clear-sky times and for~~  
397 ~~this channel is approximately 0.3 K (but during periods with liquid-bearing clouds overhead, in a~~  
398 one-hour sliding window through all data points of a day. (It also could be computed as the  
399 standard deviation of the 30 GHz-Tb is markedly higher than this threshold duedifference  
400 between Tb and the smoothed Tb to the non-homogeneous nature of clouds and thus their  
401 contribution to the downwelling microwave radiance).~~eliminate daily temperature variability.)~~  
402 Four clear-sky days ~~were selected,~~have been chosen using a criterion of 0.3 K uncertainty in the  
403 30 GHz channel: March 10 and 30, and April 13 and 29-, 2015. During periods with liquid-  
404 bearing clouds overhead, this criterion is markedly higher (more than 0.7 K) and much higher  
405 for the rainy periods (> 4 K). While those calculations were applied on a daily basis, it is  
406 important to mention that the days are not uniform in terms of cloudiness or rain. Therefore,  
407 we used the data for 2-3 hours around the time of radiosonde launches to determine to which  
408 category a particular radiosonde profile belongs, clear-sky, cloudy or rain. In this way, we found  
409 that from 58 radiosonde launches used in our statistical analysis, 41 belong to the clear-sky  
410 category, 12 - to cloudy but non-precipitating conditions, and 5 - to rainy periods. For the four  
411 chosen clear-sky days not only were the daily uncertainties of 30 GHz Tb below 0.3 K, but both  
412 sets of uncertainties described above were extremely similar with the averaged difference less  
413 than 0.05 K.

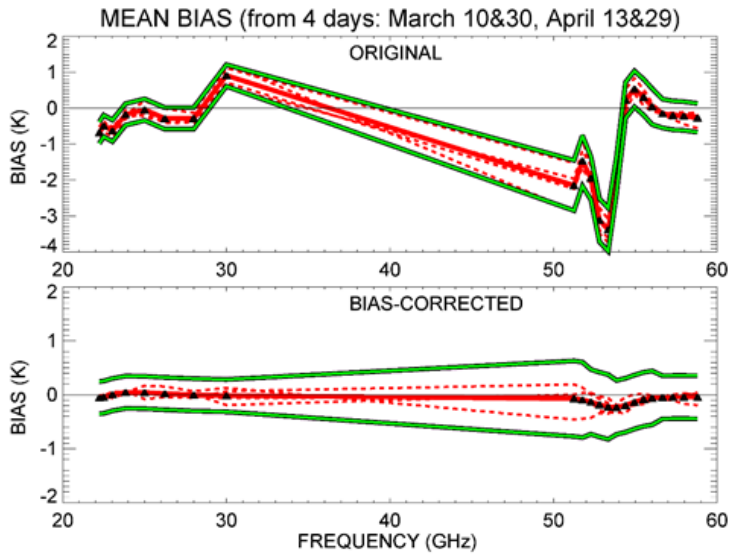
414 The bias was ~~then~~ computed ~~on all~~ for each of the 22 channels as the averaged  
415 difference between the observed Tb from the MWR zenith observations, and the forward  
416 model calculation applied to the prior, over these selected clear-sky days, and then  
417 subsequently removed from all ~~measurements~~ of the observations. We compute the bias in the  
418 bias-correction procedure only from the zenith scans, assuming that the same bias is suitable  
419 for other scans. Also, we assume that the true bias is an offset that is nearly independent of the  
420 scene, so that the sensitivity to the scene (e.g., clear or cloudy, zenith or off-zenith) is small. To  
421 investigate that, we eliminated the radiosondes launched during rainy periods (5 out of 58  
422 cases) and found that the average temperature profiles were very little different than when all  
423 radiosonde profiles were used, with the maximum bias and RMSE absolute differences 0.12 K  
424 and 0.11 K respectively up to 5 km AGL. Fig. 1 shows the results of the bias-correction for the  
425 four chosen clear-sky days. The green lines on this figure indicate the MWR random errors ~~at~~  
426 ~~each frequency calculated as the standard deviation of Tb averaged over one-hour sliding~~  
427 ~~window~~; these are 0.3-0.4 K for K-band channels and 0.64-0.7 K for V-band channels.

**Formatted:** Font color: Black

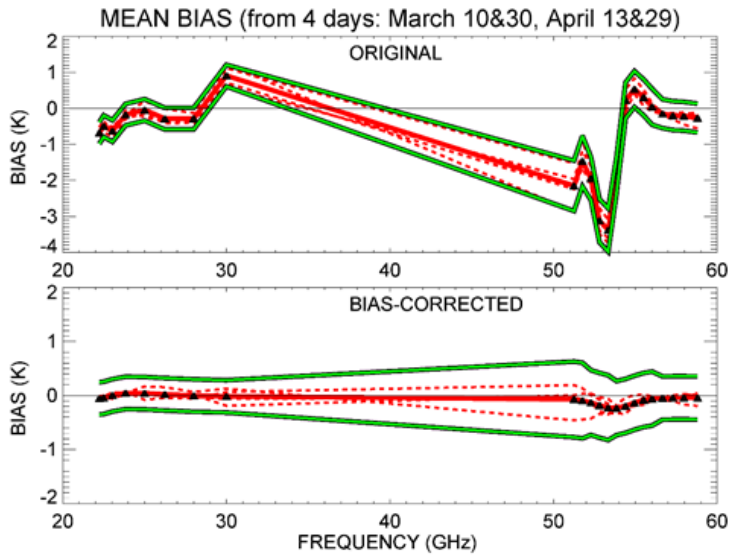
**Formatted**

**Formatted:** Space After: 12 pt, Line spacing: Double, Border: Top: (No border), Bottom: (No border), Left: (No border), Right: (No border), Between : (No border)

428



429



**Formatted:** Space After: 12 pt, Line spacing: Double, Border: Top: (No border), Bottom: (No border), Left: (No border), Right: (No border), Between : (No border)

430 Fig.1. Bias for the four chosen clear-sky days (red-dashed lines) and their mean (red solid line)  
431 for the original observations in the top panel, and for the bias-corrected data in the bottom  
432 panel. Green lines are the uncertainty boundaries around the mean bias. Frequencies used in the  
433 PR algorithm are marked with black triangles in both panels.

434  
435 This bias correction was applied to the brightness temperature used in the PR approach;  
436 however, the NN retrievals used the uncorrected brightness temperature, since it was non-  
437 trivial for us to reprocess those retrievals.

438 The retrieved profiles of the four different PR configurations presented in Table 1  
439 (MWRz, MWRzo, MWRzo915, MWRzo449) were compared to the radiosonde profiles, as well  
440 as to the NN retrievals. BAO tower temperature and mixing ratio data at the seven available  
441 levels were used as an additional validation dataset, without any interpolation.

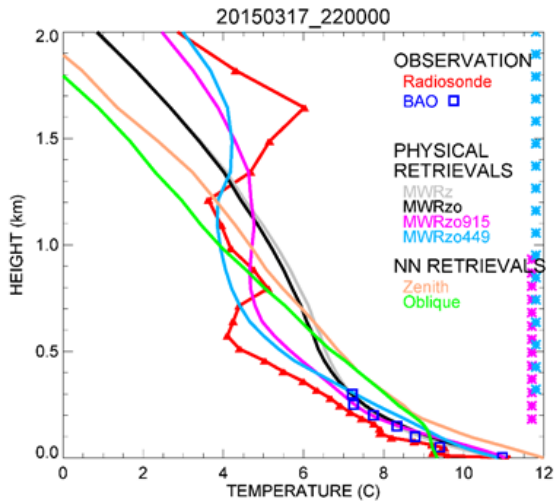
442 To compare radiosonde observations against the PR and NN retrieved profiles, all these  
443 profiles were interpolated vertically to the same PR heights, and PR and NN profiles were  
444 averaged in the time window between 15 minutes before and 15 minutes after each  
445 radiosonde launch. Since the radiosonde ascends quite quickly in the lowest kilometers of the  
446 atmosphere (~15-20 min to reach 5 km), we estimated that the 30-minute temporal window is  
447 representative of the same volume of the atmosphere measured by the radiosonde.

448 An example of the different temperature retrievals and their relative performance, data  
449 obtained on 17 March 2015 at 2200 UTC is presented in Fig. 2. Temperature profiles up to 2 km

Formatted: Indent: First line: 0"

Formatted: Space After: 12 pt, Line spacing: Double, Border: Top: (No border), Bottom: (No border), Left: (No border), Right: (No border), Between : (No border)

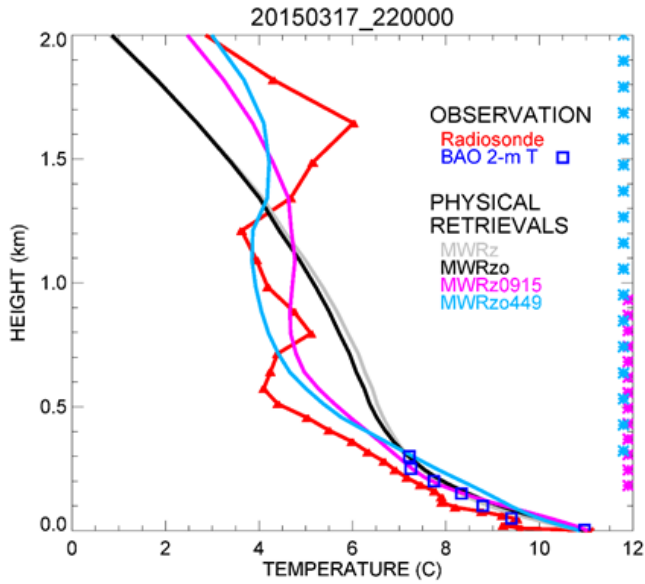
450 AGL from the four PR configurations (MWRz, MWRzo, MWRzo915, MWRzo449) are compared  
 451 to the radiosonde data in red, and to the BAO measurements in blue squares, and to the NN  
 452 profiles (NN zenith in beige, and NN oblique in green). The MWRz and MWRzo profiles, as well  
 453 as those from the NNs, are very smooth and depart quite substantially from the radiosonde  
 454 measurements, being unable to reproduce the more detailed structure of the atmospheric  
 455 temperature profile measured by the radiosonde, while the MWRzo449 profile (in light-blue)  
 456 demonstrates a better agreement with both the radiosonde and BAO measurements (blue  
 457 squares). Note that all four of the PRs match the BAO observations reasonably well, while the  
 458 NN retrievals are warm-biased. The MWRzo915 profile (in magenta) also tries to follow the  
 459 elevated temperature inversion observed by the radiosonde, successfully only in the lower part  
 460 of the atmosphere (below 1 km AGL) where RASS 915 measurements are available. This  
 461 behavior will be also addressed in the following section and in the statistical analysis presented  
 462 later in the manuscript.



463

**Formatted:** Space After: 12 pt, Line spacing: Double,  
 Border: Top: (No border), Bottom: (No border), Left: (No  
 border), Right: (No border), Between : (No border)





464  
 465 Fig. 2. Temperature profiles obtained by the four PR configurations: MWRz in gray, MWRzo in  
 466 black, MWRzo915 in magenta, and MWRzo449 in light-blue; NN retrievals: NN-zenith in beige,  
 467 and NN-averaged-oblique in green. These retrievals are compared to radiosonde  
 468 measurements, in red, and BAO tower observations, in blue squares. The heights with available  
 469 RASS virtual temperature measurements (RASS 915 in magenta and RASS 449 in light-blue), are  
 470 marked by the asterisks on the right Y-axis.

471  
 472 **3.3 Averaging kernel**

473 The averaging kernel, **Akernel** (Masiello et al., 2012, Turner and Löhnert, 2014) from Eq.  
 474 (1) can be calculated as:

475 
$$A_{kernel} = B^{-1} K^T S_{\epsilon}^{-1} K \quad (2)$$

**Formatted:** Space After: 12 pt, Line spacing: Double,  
 Border: Top: (No border), Bottom: (No border), Left: (No  
 border), Right: (No border), Between : (No border)

476 where:

477 
$$\underline{B} = \underline{S}_a^{-1} + \underline{K}^T \underline{S}_\epsilon^{-1} \underline{K}$$

478 Both matrices, **Akernel** and **B**, have dimensions 111 x 111 in our configuration. The

479 **Akernel** ~~matrix has provides~~ useful information about the calculated retrievals, such as vertical  
480 resolution and degrees of freedom for signal at each level. Thus, the rows of **Akernel** provide  
481 the smoothing functions that have to be applied to the retrievals (Rodgers, 2000) to help  
482 minimize the vertical representativeness error in the comparison between the various retrievals  
483 and the radiosonde profiles due to very different vertical resolutions of these profiles.

484 Using the averaging kernel, the smoothed radiosonde observed profiles will be  
485 therefore computed as:

486 
$$\underline{X}_{smoothed\_sonde} = \underline{Akernel} (\underline{X}_{sonde} - \underline{X}_a) + \underline{X}_a \quad \text{---(3)}$$

487 The **Akernel** in Eq. (2) depends on the retrieval parameters (e.g., which datasets are  
488 used in the **Y** vector, the values assumed in the observation covariance matrix  $\underline{S}_\epsilon$ , and the  
489 sensitivity of the forward model (i.e., its Jacobian), etc.), so for our four PR configurations it is  
490 possible to calculate four different kernels: **A\_MWRz**, **A\_MWRzo**, **A\_MWRzo915** and  
491 **A\_MWRzo449**, respectively.

492 While the top left corner of the **Akernel** matrix (1:55, 1:55) is devoted to temperature,  
493 and it will be called **AT\_MWR** hereafter, the next (56:110, 56:110) elements are devoted to  
494 water vapor mixing ratio, and will be called **AQ\_MWR**.

**Formatted: Font: Bold**

**Formatted: Space After: 12 pt, Line spacing: Double, Border: Top: (No border), Bottom: (No border), Left: (No border), Right: (No border), Between : (No border)**

495 For each of the four **Akernels**, a smoothed radiosonde profile can be computed for each  
496 radiosonde profile using Eq. (3). In the presence of temperature inversions or other particular  
497 structures in the atmosphere these smoothed profiles can be quite different from each other  
498 and also from the original unsmoothed radiosonde profile.

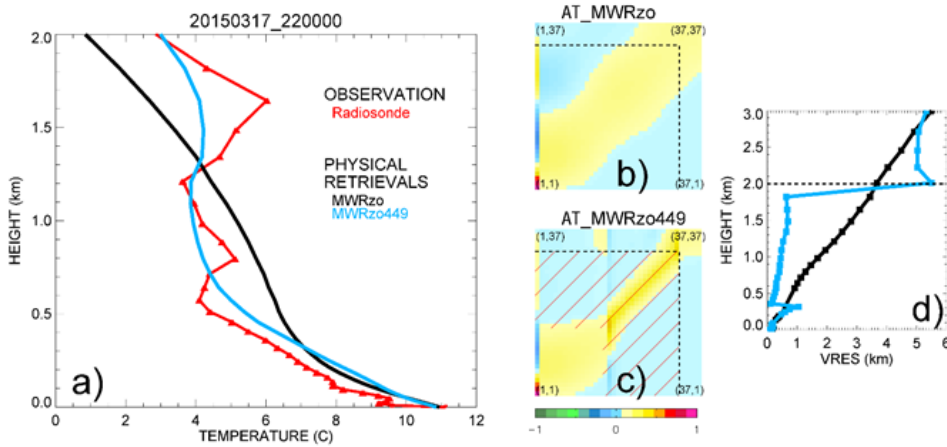
499 Therefore, in the statistical analysis presented later in the manuscript (in section 4.2),  
500 mean bias, root mean square error (RMSE), and Pearson correlation coefficients will be  
501 computed between the MWR's retrievals and both the unsmoothed and smoothed radiosonde  
502 profiles, where the latter were computed using their respective **Akernels**.- Additional  
503 observational data help to resolve the atmospheric structure in more detail, therefore we  
504 would expect to obtain better statistical evaluations from the configurations including  
505 additional RASS observations compared to the runs without RASS data.

506 The improvement in the retrieved temperature profiles presented in Fig. 2 obtained  
507 using additional RASS data can be explained and clearly shown by the **ATkernel** itself. Figure 3  
508 includes the temperature profiles of the radiosonde (unsmoothed and **ATkernel**'s smoothed)  
509 and PRs of MWRzo and MWRzo449 (panel a), and the **ATkernels** corresponding to these PRs in  
510 the color plots in the middle of the figure (panels b and c). These color plots are a schematic  
511 visualization of the 37 x 37 top left corner of the **ATkernel** matrix that illustrates the part of the  
512 **ATkernel** up to 3 km, for reference. Dash lines mark the 2 km vertical level.

513 The rows of the **ATkernel** provide a measure of the retrieval smoothing as a function of  
514 altitude, so the full-width half maximum of each **ATkernel** row estimates the vertical resolution  
515 of the retrieved solution at each vertical level (Merrelli and Turner, 2012). These plots of

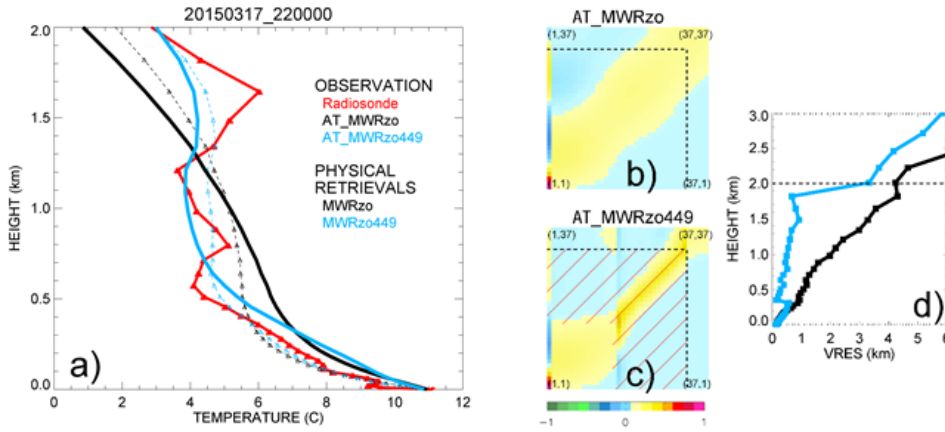
516 temperature vertical resolution vs height for MWRzo and MWRzo449 are included in  
 517 Figure 3, panel d, for the same case presented in Fig. 2. Comparison of **ATkernel** color plots and  
 518 vertical resolution plots of MWRzo vs MWRzo449 shows that additional observations from the  
 519 RASS 449 significantly reduces the spread around the main diagonal from ~200m up to 2 km (in  
 520 the layer of the atmosphere where RASS 449 measurements are available), thereby improving  
 521 the vertical resolution of the retrievals (as clearly visible in panel d).

522



523

**Formatted:** Space After: 12 pt, Line spacing: Double, Border: Top: (No border), Bottom: (No border), Left: (No border), Right: (No border), Between : (No border)



524  
 525 Fig. 3. Panel a: observed temperature profiles from radiosonde, in red, from AT kernels smoothed  
 526 radiosonde, AT MWRzo in dashed black, and AT MWRzo449 in dashed light-blue; PRs from  
 527 MWRzo PR in black, and from MWRzo449 PR in light-blue. Middle colored panels: 37x37 levels  
 528 (surface to 3 km) of the Akernel matrix for temperature, b) AT\_MWRzo and c) AT\_MWRzo449.  
 529 Right panel d: vertical resolution (VRES) as a function of the height for the MWRzo PR (black),  
 530 and for the MWRzo449 PR (light-blue). DashDashed lines on plots b)-d) mark 2 km AGL. Hatched  
 531 area on panel c) marks the RASS measurement heights.

532  
 533 **4. Results**  
 534 PR and NN retrieved profiles have been evaluated against radiosonde observations. For  
 535 additional verification, radiosonde data from 59 launches taken between 9 March and 4 May  
 536 2015 were first of all compared to the BAO tower measurements, up to 300 m AGL. These  
 537 observed data sets match very well, with a correlation coefficient of 0.99 and a standard

**Formatted:** Outline numbered + Level: 1 + Numbering Style: 1, 2, 3, ... + Start at: 1 + Alignment: Left + Aligned at: 0.25" + Indent at: 0.5"

**Formatted:** Space After: 12 pt, Line spacing: Double, Border: Top: (No border), Bottom: (No border), Left: (No border), Right: (No border), Between: (No border)

538 deviation of  $\sim 0.7$   ~~$^{\circ}\text{K}$~~  $^{\circ}\text{C}$ . However, one radiosonde profile showed a large bias ( $> 5$   ~~$^{\circ}\text{K}$~~  $^{\circ}\text{C}$ ) against  
539 all seven levels of BAO temperature measurements and against all PRs ~~and NNs~~, therefore we  
540 decided to exclude this particular radiosonde profile from the statistical calculations.

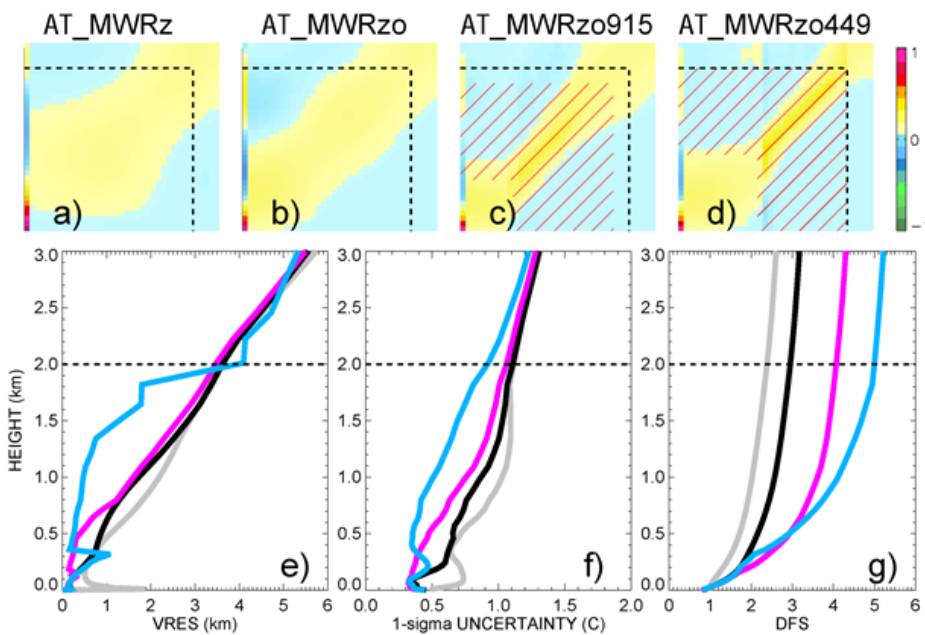
541

#### 542 **4.1 ~~PRs~~Physical retrieval statistical analysis from Akernel**

543 To complete the analyses on the **ATkernel** changes and dependencies from different  
544 types of observational data used in the PRs, the **ATkernels**, averaged over all radiosonde  
545 events, are shown in Fig. 4, panels a-d, for the four PR configurations of Table 1, in the same  
546 way as shown in Fig. 3, b-c. A clearly visible gradual narrowing of the spread around the main  
547 diagonal is obtained by the usage of the additional observations, from MWR zenith only (panel  
548 a), to MWR zenith-oblique (panel b), to the larger impact obtained by the usage of RASS 915  
549 (panel c) and RASS 449 (panel d) data.

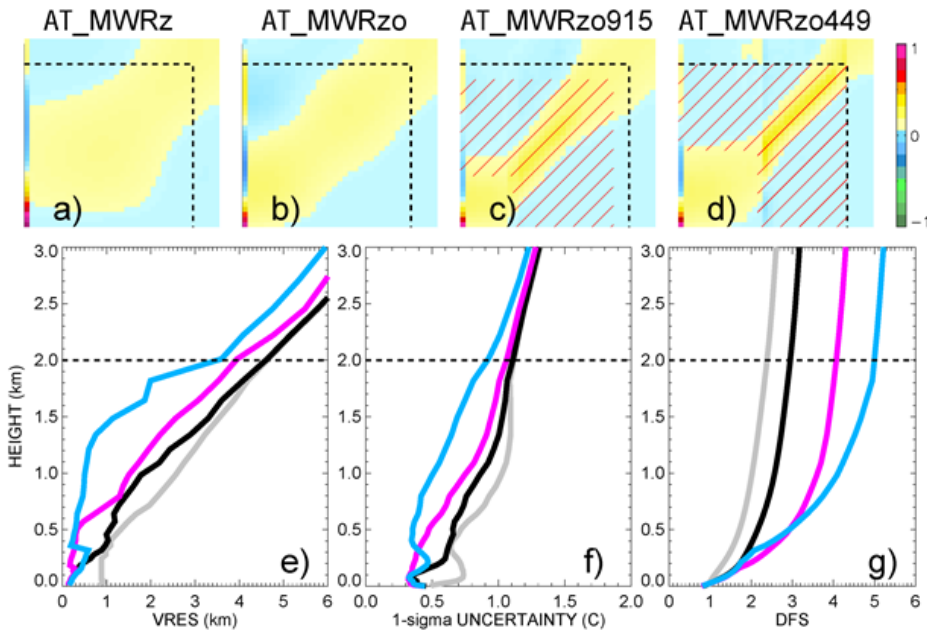
550 Other statistically important features to analyze in the PRs, besides vertical resolution,  
551 are the retrieval uncertainty, and the degree of freedom for signal (DFS). These three features  
552 are also shown in Fig.4, panels e-g, at each of the heights of the retrieved solution, up to 3 km  
553 AGL, and averaged over all radiosonde events. While the vertical resolution (panel e) shows the  
554 width of the atmosphere layer used for each retrieval height (the vertical resolution is  
555 computed as the full-width half-maximum (FWHM; Maddy and Barnet, 2008) value of the  
556 averaging kernel), the uncertainty (panel f) gives a measure of the retrieval correctness  
557 (computed by propagating the uncertainty of the observations and the sensitivity of the  
558 forward model), and the DFS (panel g) is a measure of the number of independent pieces of

559 information used in the retrieved solution. For example, at the 1 km AGL level the vertical  
 560 resolution of MWRzo449 equals 0.5 km, i.e. information from +/- 0.5 km around the retrieval  
 561 height are considered in the retrieval, while all other retrievals use the information from +/- 2  
 562 km. Also, the uncertainty of the MWRzo449 retrieval up to ~~1 km~~ 1 km AGL is around 0.5 °K°C  
 563 while the other retrievals have higher uncertainties of up to 1 °K°C. The higher accuracy of the  
 564 MWRzo449 retrievals is because they use more observational information compared to the  
 565 other retrieval configurations.



566

**Formatted:** Space After: 12 pt, Line spacing: Double,  
 Border: Top: (No border), Bottom: (No border), Left: (No  
 border), Right: (No border), Between : (No border)



567  
 568 Fig. 4. Top four-color images: **AT** kernels for MWRz (panel a), MWRzo (panel b), MWRzo915  
 569 (panel c) and MWRzo449 (panel d), averaged over all radiosonde events. Hatched area on  
 570 panels c) and d) marks the RASS measurement heights. Bottom three panels from left to right:  
 571 vertical resolution (VRES) in km (panel e), one-sigma uncertainty derived from the posterior  
 572 covariance matrix in °C (panel f), and cumulative Degree of Freedom (DFS, panel g) as a function  
 573 of height for temperature, averaged over all radiosonde events (MWRz is in gray, MWRzo is in  
 574 black, MWRzo915 is in magenta, and MWRzo449 is in light-blue). ~~Dash~~Dashed lines mark 2 km  
 575 AGL on all panels.

576

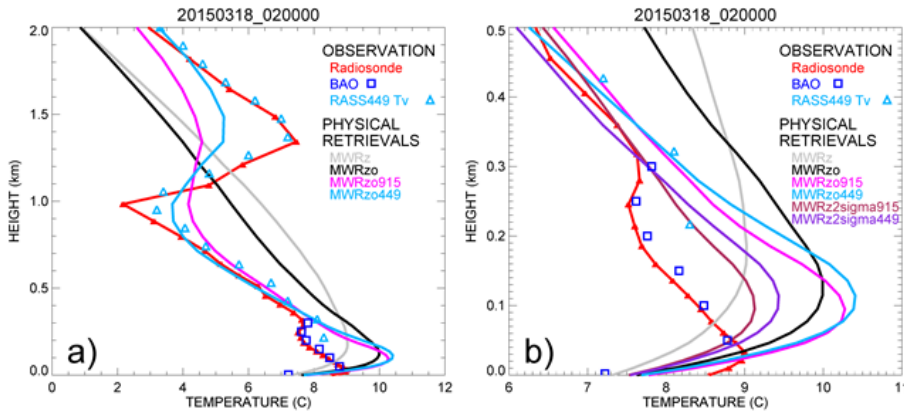
**Formatted:** Space After: 12 pt, Line spacing: Double,  
 Border: Top: (No border), Bottom: (No border), Left: (No  
 border), Right: (No border), Between : (No border)



577 The improvements from MWRz (in gray) to MWRzo (in black), then to MWRzo915 (in  
578 magenta), and finally to MWRzo449 (in light-blue) are visible in all three panels (Fig 4 e-g),  
579 whereas MWRzo449 has the best statistical measures compared to the other PRs, particularly  
580 below 2 km AGL, where RASS 449 measurements are available. Finally, it is interesting that  
581 below 200 m AGL the MWRzo915 has slightly better statistics compared to the MWRzo449, as  
582 could be expected due to the first available height of the RASS 915 being lower (120 m AGL)  
583 than the first available height for the RASS 449 (217 m AGL) and due to the finer vertical  
584 resolution of the 915-MHz RASS. This suggests that if additional observations were available in  
585 the lowest several 100 m ~~layer~~ of the atmosphere where RASS measurements are not available,  
586 improvements might be even better closer to the surface, where temperature inversions, if  
587 present, are sometimes difficult to retrieve correctly.

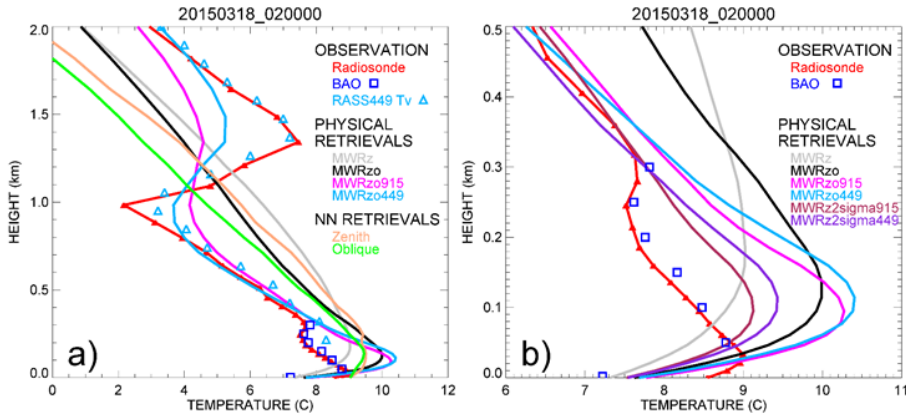
588 As a matter of fact, we found several cases during XPIA when the temperature profile  
589 exhibits inversions, with the lowest happening in the surface layer. Figure 5a shows one of the  
590 most complex cases, with several temperature inversions visible in the temperature profile  
591 from the radiosonde (red line), in the temperature measurements from the BAO tower (blue  
592 squares), and in the virtual temperature measured by the RASS 449 (light blue triangles). We  
593 note that the virtual temperature profile is in close agreement with the temperature measured  
594 by radiosonde. Generally, the moisture contribution to the virtual temperature is less than a  
595 degree K, decreasing substantially for dryer air. Among the PR profiles, the PRs including RASS  
596 data show better agreement with the radiosonde in the atmospheric layer where RASS  
597 measurements are available, as ~~was already~~ shown in Fig. 2 for a different date. Unfortunately,

598 this better performance is not visible below the first available RASS measurement, i.e. from the  
599 surface up to ~200m AGL, where the PRs with additional RASS data have the largest positive  
600 bias compared to both radiosonde and BAO data in this layer. We believe that the MWR  
601 data, especially those from the oblique scans, in this case have a bias in the observed brightness  
602 temperatures that propagates through the retrieval calculations, and including other  
603 observational data is not enough to correct it in the layer between the surface data and the first  
604 available RASS measurement.



605

**Formatted:** Space After: 12 pt, Line spacing: Double, Border: Top: (No border), Bottom: (No border), Left: (No border), Right: (No border), Between : (No border)



606  
 607 Fig. 5. Panel a) as in Fig. 2 but for 18 March 2015 at 0200 UTC. The RASS 449 virtual  
 608 temperature is included as light blue triangles. Panel b) shows the same data (except for the NN  
 609 retrievals) presented in panel a) but only up to 500 m AGL, and includes PR profiles in which the  
 610 MWR uncertainties were increased by a factor of two, MWRz915 in maroon and MWRz449 in  
 611 violet.

612  
 613 After several trials, we found that when RASS measurements are included, temperature  
 614 profiles in this and similar cases exhibiting inversions could be improved -by increasing the  
 615 random uncertainty of MWR observations, and only using the zenith MWR measurements,  
 616 because the oblique MWR brightness temperature measurements (which give more  
 617 information in the lower layer of the atmosphere) seemingly have a bias that competes with  
 618 the active and more accurate measurements from the RASS and surface observations. In this  
 619 way, the PR approach is granted more freedom to get an optimal profile in the gap between the

**Formatted:** Space After: 12 pt, Line spacing: Double,  
 Border: Top: (No border), Bottom: (No border), Left: (No  
 border), Right: (No border), Between : (No border)

620 lowest RASS measurements and the surface measurement. Proof of this is presented in Figure  
621 5b, that shows the same data as in 5a, but including the profiles obtained when increasing the  
622 assumed MWR Tb uncertainties by a factor of two, hereafter called MWRz2sigma915 and  
623 MWRz2sigma449, in maroon and violet respectively. The increased accuracy of these  
624 temperature profiles compared to MWRzo915 and MWRzo449 are obvious in the layer of  
625 atmosphere closer to the surface. Later we will show that these last two PR configurations  
626 demonstrate improved statistics over all 58 cases, and also through the layer of the atmosphere  
627 up to ~~5km~~5 km. We note that these last two PR configurations, that were found to work well  
628 for this dataset, might not be optimal for other datasets. During XPIA the RASS measurements  
629 impact (particularly those from the RASS 449) was important in the PR approach. This might not  
630 be the case for other datasets or over different seasons, when RASS coverage might not be as  
631 good as ~~that~~ during XPIA. For this reason, we think that attention has to be used to determine  
632 what is the best configuration to use when dealing with PR approaches. On the positive side,  
633 the advantage is that the user can determine and has control on what is the optimal  
634 configuration to use in his/her dataset, in terms of different inputs to employ and their relative  
635 uncertainty.

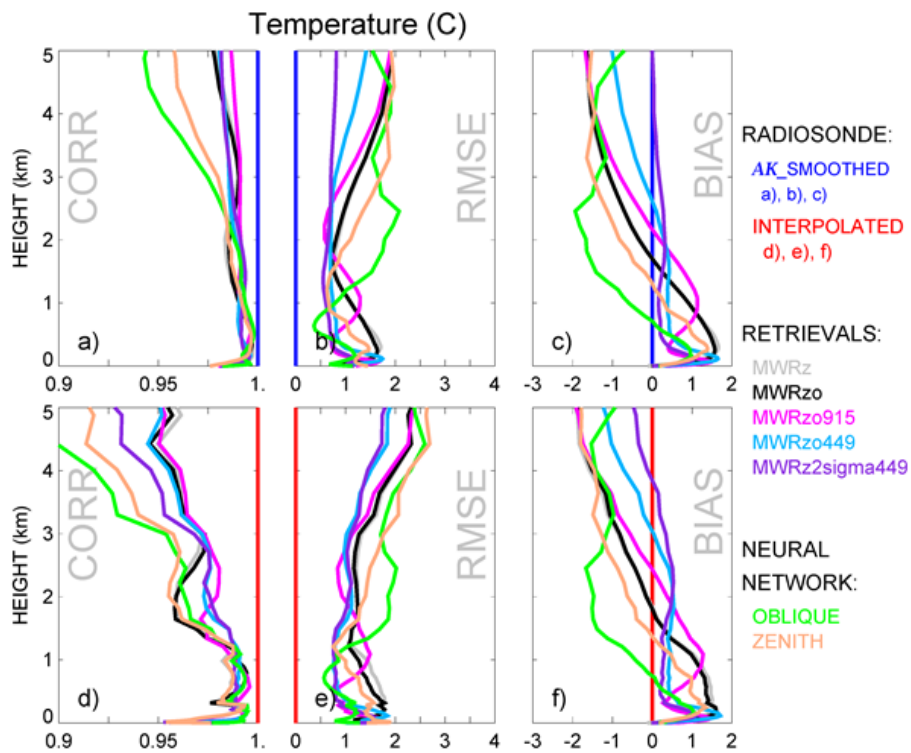
636

#### 637 **4.2 Statistical analysis of ~~PRs compared to NN~~physical retrievals up to 5km AGL**

638 ~~Since the iteratively~~We calculated PRs and the NN retrievals are obtained by very  
639 ~~different approaches, we find it very important to compare their~~the relative statistical  
640 behavior. ~~We do this of PRs for both~~ ~~for~~ temperature and mixing ratio, providing ~~this~~the  
641 comparison in two ways: first ~~using~~to the ~~kernel~~ smoothed radiosonde ~~data obtained using~~

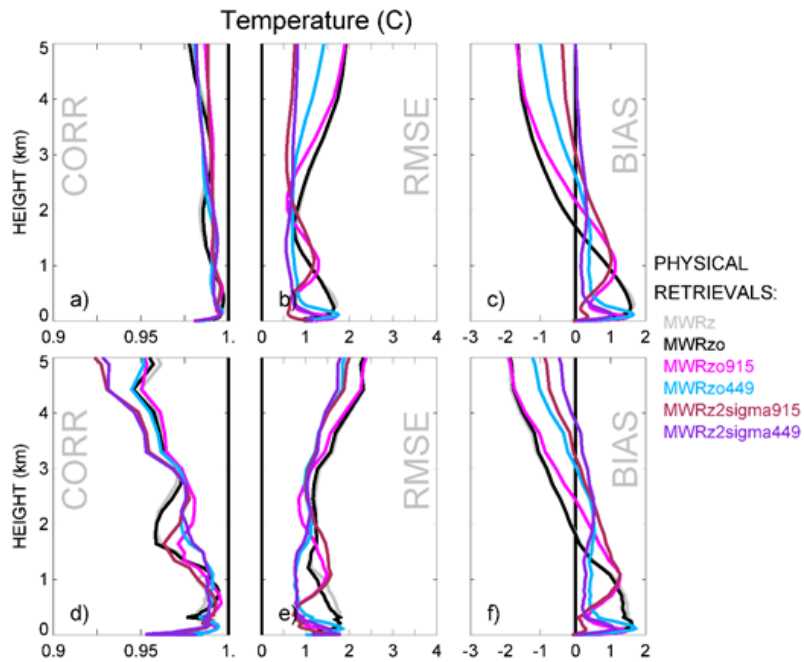
642 the averaging kernel matrix (as described in section 3.3.7), and second comparing to the original,  
643 unsmoothed, radiosonde profiles, just interpolated to the 55 PR vertical levels.

644 Figure 6 shows the statistical results of these comparisons for temperature, in terms of  
645 Pearson correlation, RMSE, and mean bias, averaged over all radiosonde events.



646

**Formatted:** Space After: 12 pt, Line spacing: Double,  
Border: Top: (No border), Bottom: (No border), Left: (No  
border), Right: (No border), Between : (No border)



647

648 Fig. 6. Pearson correlation, RMSE, and mean bias for temperature profiles of MWRz in gray,  
 649 MWRzo in black, MWRzo915 in magenta, MWRzo449 in light-blue, MWRz2sigma915 in maroon  
 650 and MWRz2sigma449 in violet, computed comparing to smoothed radiosonde data (using their  
 651 relative **ATkernel**) in panels a-c, and against the original radiosonde measurements in panels d-  
 652 f. *The same comparisons for NN profiles, with NN zenith in beige, and NN averaged oblique in*  
 653 *green, are made against the corresponded smoothed radiosonde data in the top panel and*  
 654 *against original radiosonde data in the bottom panel.*

655

**Formatted:** Space After: 12 pt, Line spacing: Double,  
 Border: Top: (No border), Bottom: (No border), Left: (No  
 border), Right: (No border), Between : (No border)

656 These results confirm the superiority of the MWRz2sigma449 temperature retrieval  
657 over the other PRs. While this is not true at all heights, this retrieval shows improved  
658 distribution of RMSE and bias for the atmospheric layer up to 5 km AGL. The differences  
659 between the MWRz2sigma915 profile is not included in the figure to not overcrowd it, but its  
660 behaviour compared to and the MWRzo915 is profiles are similar to that of those between the  
661 MWRz2sigma449 compared to and the MWRzo449 profile profiles, reducing the drastic bias  
662 found in the layer closer to the ground. The differences between the two ways of comparison,  
663 against the smoothed **ATkernel** or the original radiosonde data, are small in terms of RMSE and  
664 bias, but more evident in terms of correlation as ~~it~~ can be expected because of the smoothing  
665 technique applied to the radiosonde profiles through Eq. (3). Above and below ~1.56 km AGL  
666 the bias, RMSE, and correlation profiles of the PRs show very different behavior. While  
667 statistical ~~measures~~ scores above ~1.56 km AGL are very similar for the four PRs introduced in  
668 Table 1, they are better for the MWRz2sigma915 and MWRz2sigma449 PRs, especially when  
669 compared to the smoothed radiosonde profiles. Differences between the profiles show more  
670 variability in the lowest 1.5 km. NN retrievals, both for zenith and averaged oblique, are very  
671 variable from height to height and generally have much larger RMSE and bias, and worse  
672 correlation coefficients compared to PRs. ~1.6 km where most of the active RASS measurements  
673 are available. Also, while both PR profiles related to the RASS 449, MWRzo449 and  
674 MWRz2sigma449, have almost constant bias and RMSE from 200m up to at least 3 km, the  
675 RASS 915 based PR profiles, MWRzo915 and MWRz2sigma915, have biases and RMSEs that  
676 vary with height. Due to the lower first range gate of the RASS 915 measurements, the PR  
677 profile of MWRz2sigma915 has the smallest bias and RMSE compared to all other PR profiles in

678 the surface to 200 m layer. With quickly decreasing availability of RASS 915 measurement  
679 above this layer, the bias and RMSE of MWRzo915 and MWRz2sigma915 became larger, and in  
680 some higher layers even larger than the corresponding statistical measures of MWRz and  
681 MWRzo. This marks the importance of active measurements spanning a prominent vertical  
682 layer to provide a useful application of these data in a radiative transfer model.

683 Besides temperature profiles, the ~~NN and~~ PR retrievals also provide water vapor mixing  
684 ratio profiles. - It is understandable that the different configurations of PRs are not noticeably  
685 different from each other in relation to moisture, because the Tv observations from the RASS  
686 are dominated by the ambient temperature (not moisture), and thus have little impact on the  
687 water vapor retrievals.

688 -Figure 7 includes the two **AQ** kernels corresponding to the PRs MWRz and MWRzo449  
689 in panels a and b, which are averaged over all radiosonde events and appear to be almost  
690 identical. More detailed statistical estimations of PRs mixing ratio in Fig 7 c-e, also averaged  
691 through all radiosonde events, show very similar correlations, RMSEs, and biases for all PRs  
692 included in the figure, meaning that the impact of including RASS observations is minimal on  
693 this variable. ~~These PR mixing ratio profiles are also statistically very close to the averaged~~  
694 ~~oblique NN retrieval mixing ratio profiles, with the zenith NN retrieval mixing ratio profiles~~  
695 ~~showing the worst statistics in terms of RMSE and bias. Overall, we conclude that the PR~~  
696 ~~retrievals are not degraded on average compared to the NN moisture retrievals.~~

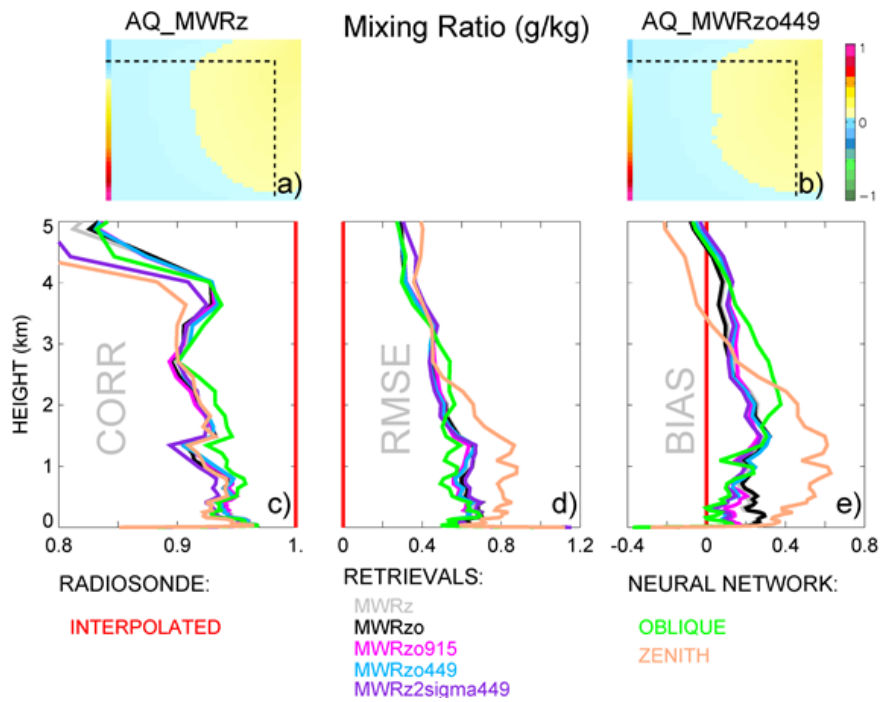
697



698

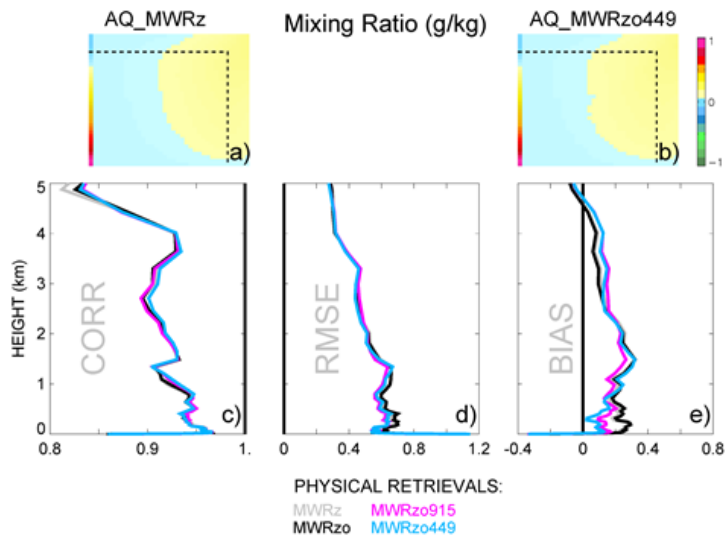
699

**Formatted:** Space After: 12 pt, Line spacing: Double, Border: Top: (No border), Bottom: (No border), Left: (No border), Right: (No border), Between : (No border)



700

**Formatted:** Space After: 12 pt, Line spacing: Double, Border: Top: (No border), Bottom: (No border), Left: (No border), Right: (No border), Between : (No border)



701

702 Fig. 7. Top two-color images: **AQ** kernels for MWRz (panel a) and MWRzo449 (panel b),  
 703 averaged over all radiosonde events and shown up to 3 km AGL with dash lines mark 2 km AGL  
 704 on both panels. Bottom three panels are the same as panels d-f in Figure 6, but for mixing ratio  
 705 estimation.

706

707 **4.3 Statistics for cases far from the climatological mean**

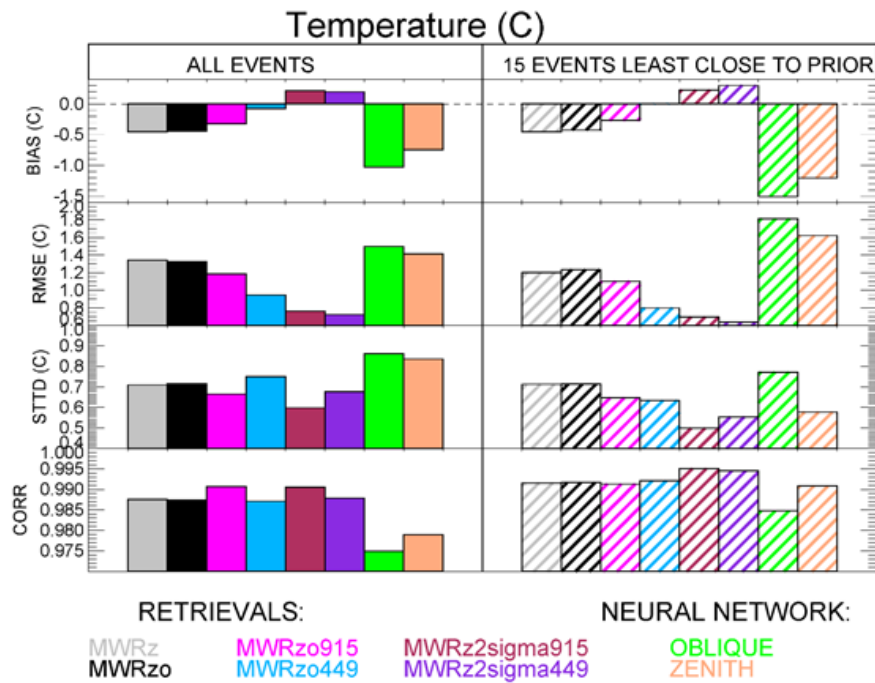
708 ~~While both approaches, physical and neural network retrievals, are quite different,~~  
 709 ~~both~~ Physical retrievals use climatological data as a constraint or for building the statistical  
 710 relationships used in the retrieval. Statistically, the averaged profiles of both temperature and  
 711 moisture variables are very close to the climatological averages. However, the most interesting

**Formatted:** Space After: 12 pt, Line spacing: Double,  
 Border: Top: (No border), Bottom: (No border), Left: (No  
 border), Right: (No border), Between : (No border)

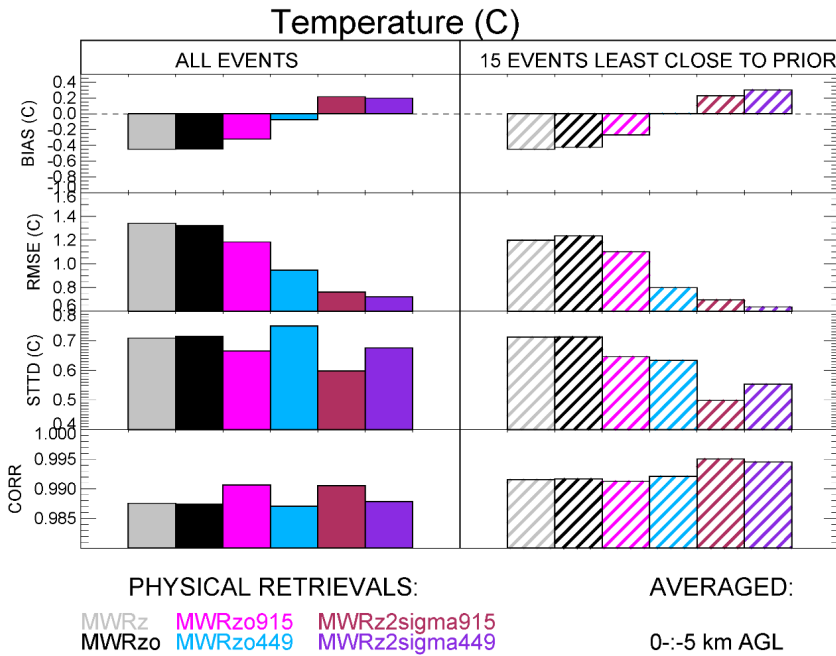
712 and difficult profiles to retrieve are the cases furthest from the climatology (Löhnert and Maier,  
713 2012). To check the behavior of the retrieved data in such events, we first calculated the RMSE  
714 for each radiosonde profile relative to the prior profiles for 42 vertical levels from the surface  
715 up to 5 km AGL, and then we selected the 15 cases with the largest 0-5km layer averaged  
716 RMSEs compared to the prior. All comparisons are done against the corresponded smoothed  
717 **ATkernel** radiosonde data, using **AT\_MWRz, AT\_MWRzo, AT\_MWRzo915, AT\_MWRzo449,**  
718 **AT\_MWRz2sigma915, AT\_MWRz2sigma449** for all six PRs, ~~and **AT\_MWRz, AT\_MWRzo** for NN~~  
719 ~~zenith and NN-oblique retrievals respectively.~~

720

**Formatted:** Space After: 12 pt, Line spacing: Double,  
Border: Top: (No border), Bottom: (No border), Left: (No  
border), Right: (No border), Between : (No border)



**Formatted:** Space After: 12 pt, Line spacing: Double, Border: Top: (No border), Bottom: (No border), Left: (No border), Right: (No border), Between : (No border)



722

723

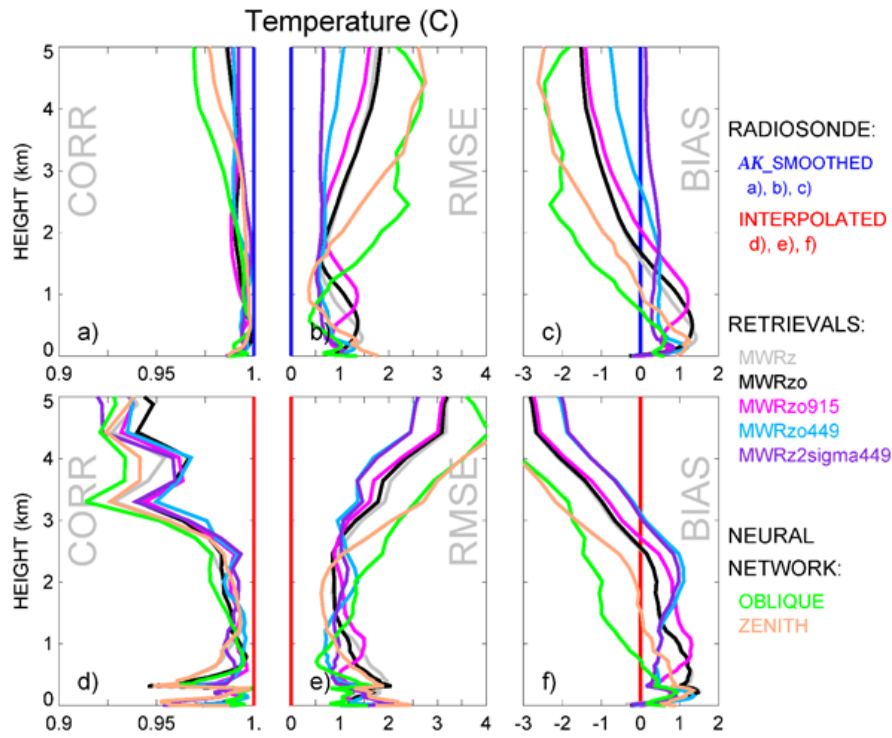
724 Fig. 8. From top to bottom: biases (retrievals minus ATkernel radiosonde), RMSEs, standard  
 725 deviations of the difference between retrievals and ATkernel radiosonde, and Pearson  
 726 correlations for the six PR configurations so far introduced ~~and both NN retrievals~~, averaged  
 727 from the surface to 5 km AGL, averaged over all radiosonde data (solid boxes), and averaged  
 728 over the 15 events furthest from the priors (hatched boxes).

729

730 Figure 8 shows the temperature statistical analysis for the entire radiosonde data set  
 731 (solid boxes) and to just the fifteen chosen events (hatched boxes) for bias, RMSE, standard  
 732 deviation of retrieval differences to the radiosonde data, and Pearson correlation, calculated as

**Formatted:** Space After: 12 pt, Line spacing: Double,  
 Border: Top: (No border), Bottom: (No border), Left: (No  
 border), Right: (No border), Between : (No border)

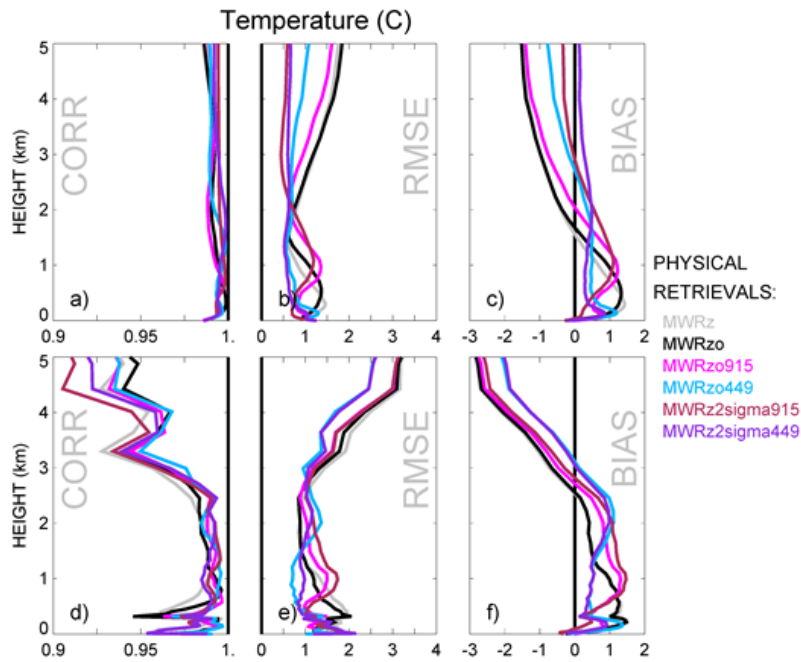
733 the weighted averaged over the 42 vertical heights up to 5 km AGL. The vertical resolution of  
734 the Physical Retrievals is not uniform, with more frequent levels closer to the surface. If a  
735 simple average of the data from all levels is used, the near-surface layer will be weighted more  
736 compared to the upper levels of the retrievals. To avoid this, a vertical average over the lowest  
737 5km AGL is performed using weights at each vertical level determined by the distance between  
738 the levels. Differences in the statistics when using the entire radiosonde data set or the fifteen  
739 profiles furthest from the prior are noticeable, especially for bias and RMSE, but also for the  
740 standard deviation. All PRs that include RASS observations show better performance compared  
741 to strictly MWR-only PR profiles (i.e., MWRz and MWRzo) for almost all statistical comparisons.  
742 Also, the statistical behavior of the MWRz2sigma915 and MWRz2sigma449 retrievals are the  
743 best in terms of RMSE and standard deviation for all events and for RMSE, standard deviation,  
744 and correlation coefficient, for the fifteen profiles furthest from the climatological average. Fig.  
745 Finally, we note8 also shows that the NN profiles are the least accurate retrievals for all of the  
746 statistics for the entire radiosonde data set, RMSE, standard deviation and have the highest  
747 bias, RMSE and the lowest correlation have improved scores for the 15 events furthest from the  
748 prior when compared to all temperature profiles for all PRs using active RASS measurements.



749

**Formatted:** Space After: 12 pt, Line spacing: Double, Border: Top: (No border), Bottom: (No border), Left: (No border), Right: (No border), Between : (No border)





750  
 751 Fig. 9. The same as Fig. 6 but for the temperature over 15 furthest from prior radiosonde  
 752 profiles.

753  
 754 To investigate the vertical structure of the error statistics for the 15 events furthest from  
 755 the radiosonde climatology, profiles of correlation, RMSE and bias for these events are shown  
 756 in Figure 9 for the layer 0-5 km. -The ~~MWRz449~~MWRz2sigma915 and MWRz2sigma449 profiles,  
 757 ~~which were seen in having Fig. 8 to have~~ the best layer-averaged statistics in Fig. 8, are seen to  
 758 ~~be~~ as good as, or better, than the other methods for the 0-2 km layer.- Importantly, for heights  
 759 above 2km AGL, where there is no additional observational data from RASS, all of the PRs are

**Formatted:** Space After: 12 pt, Line spacing: Double,  
 Border: Top: (No border), Bottom: (No border), Left: (No  
 border), Right: (No border), Between : (No border)

760 better than the NN profiles, with the MWRz2sigma449 and MWRz449 being the best. We note  
761 that the increased accuracy of the PRs relative to the NNs is more obvious in Fig. 9 for the 15  
762 events when compared to the entire data set in with RASS are closer to the “true” radiosonde  
763 temperature compared to the PRs without RASS. Fig. 6. Also, it can be seen that the NNs for the  
764 15 events are worse than they are for the entire data set, especially in the 2-5km layer, which  
765 indicates (not surprisingly) that the NNs accuracy degrades when the atmosphere is far from its  
766 climatology.

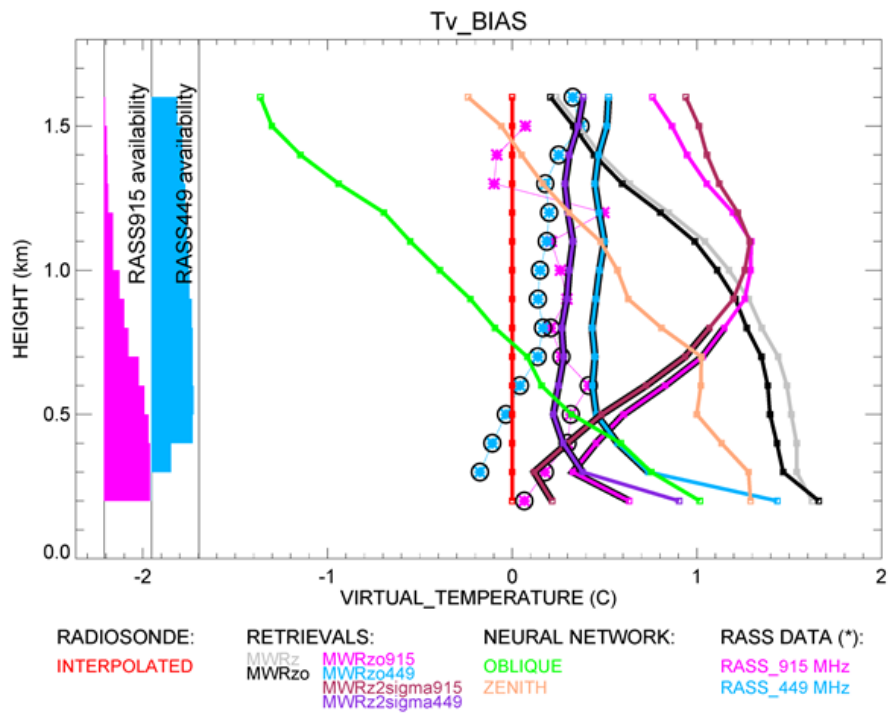
767

#### 768 4.4 Virtual temperature statistics

769 The above analysis confirms the superiority of MWRz2sigma915 and MWRz2sigma449  
770 compared to the other PRs ~~and to the NN retrievals~~ for this dataset. In this section we show the  
771 direct comparison of the retrieved profiles to the original radiosonde and RASS virtual  
772 temperature profiles. Using temperature and moisture retrieval output, we calculated  
773 “retrieved virtual temperature profiles” and interpolated all profiles and RASS data on a regular  
774 vertical grid, going from 200 m to 1.6 km with 100 m range, for easy comparison.

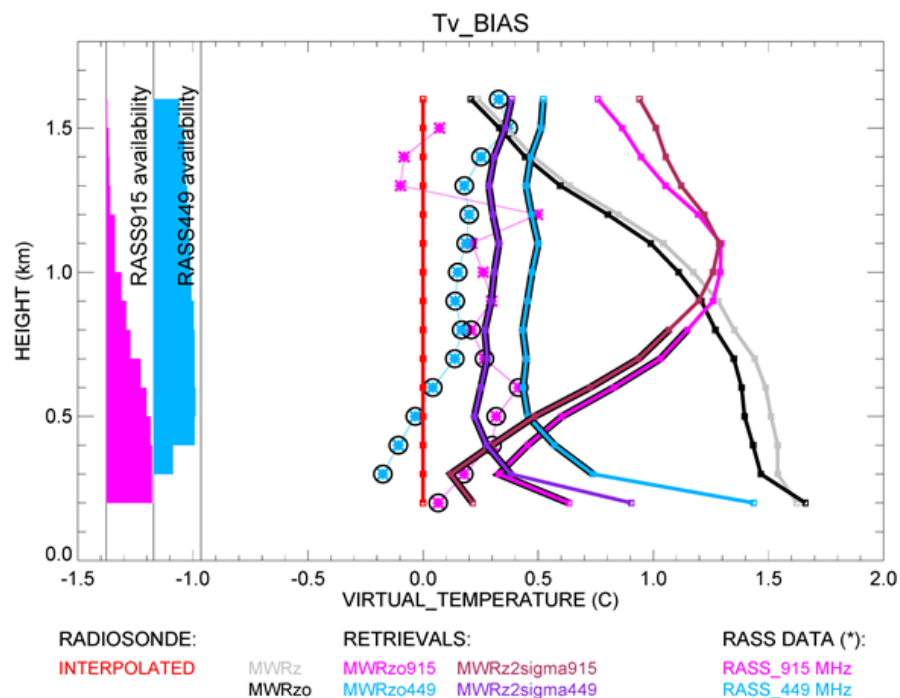
775 Figure 10 shows Tv retrieved profile biases compared to the original radiosonde data as  
776 solid lines, and RASS 915 and RASS 449 Tv bias as asterisks. A zero bias is denoted by the red  
777 line. On the left side of the figure we show bar charts of the RASS measurement availability as a  
778 function of height. The widest part of these charts corresponds to 100% data availability.  
779 Heights with RASS availability greater than 50% are marked with additional circles over the  
780 asterisks.

**Formatted:** Space After: 12 pt, Line spacing: Double,  
Border: Top: (No border), Bottom: (No border), Left: (No  
border), Right: (No border), Between : (No border)



781

**Formatted:** Space After: 12 pt, Line spacing: Double, Border: Top: (No border), Bottom: (No border), Left: (No border), Right: (No border), Between : (No border)



782  
 783 Fig. 10. Bias of virtual temperature for all six PR configurations *and both NN retrievals*  
 784 compared to the original radiosonde measurements. RASS data are marked by asterisks and by  
 785 additional circles for the RASS data with more than 50% availability, according to the availability  
 786 bar charts on the left.

787  
 788 While RASS 449 data are available at almost all heights up to 1.6 km, the RASS 915 data  
 789 availability decreases considerably with height, lowering to 50% availability around 800 m AGL.  
 790 All PRs with input from RASS data, MWRzo915 and MWRzo449, and MWRz2sigma915 and  
 791 MWRz2sigma449 ~~with larger MWR uncertainties~~, are also marked with additional black lines at

**Formatted:** Space After: 12 pt, Line spacing: Double,  
 Border: Top: (No border), Bottom: (No border), Left: (No  
 border), Right: (No border), Between : (No border)

792 the heights with at least 50% of relative RASS data availability. This figure clearly shows the  
793 superiority of MWRz2sigma449 and MWRz2sigma915 (in the layer with > 50% RASS 915 data  
794 availability) compared to MWRz and MWRzo configurations, which do not include RASS data, as  
795 well as to MWRzo915 and MWRzo449 which include RASS data and MWR zenith and oblique  
796 data. For MWRzo449 and MWRz2sigma449 profiles, RASS 449 data were almost always  
797 available, therefore it is easy to identify similar features between Tv bias profiles of the RASS  
798 449 and the PRs including it. Thus, for the MWRzo449 and MWRz2sigma449 the Tv bias is more  
799 uniform through the heights compared to all other PRs that do not include RASS data, ~~and to~~  
800 ~~both NN retrievals.~~ Moreover, because MWRzo449 and MWRz2sigma449 Tv bias profiles  
801 follow tightly the trend of the RASS 449 with height, the difference between MWRzo449 and  
802 RASS 449 biases equals  $\sim 0.32$  °C and the difference between MWRz2sigma449 and RASS 449  
803 biases equals  $\sim 0.14$  °C over the  $\sim 1.3$  km atmospheric layer where most of RASS 449  
804 measurements are available, uniformly distributed through the heights. Finally, the average  
805 differences between these MWRzo449 and MWRz2sigma449 Tv profiles and the radiosonde  
806 virtual temperature equal  $\sim 0.56$  °C and  $\sim 0.34$  °C respectively. ~~From these results we can~~  
807 ~~assume that the final bias of the PRs that include additional RASS data derives from a~~  
808 ~~combination of the RASS data bias itself, of the uncertainty of the retrieval model, and of the~~  
809 ~~MWR brightness temperature biases, even though we tried to correct for the latter.~~

810 We note that as an alternative to using the PR ~~temperatures~~temperature profiles at all  
811 heights, one could consider replacing the PR temperatures with RASS observations up to the  
812 maximum height reached by the RASS, and then use the PR retrieval above that. -To do this the

813 moisture contribution to the RASS virtual temperatures could be removed by using either the  
814 relative humidity measured by radiometer or by a climatology of the moisture term.

815

## 816 5. Conclusions

817 In this study we used the data collected during the XPIA field campaign to test different  
818 configurations of a physical-iterative retrieval (PR) approach in the determination of  
819 temperature and humidity profiles from data collected by microwave radiometers, surface  
820 sensors, and RASS measurements. We tested the accuracy of several PR configurations, two  
821 that made use only of surface observations and MWR observed brightness temperature (zenith  
822 only, MWRz, and zenith plus oblique, MWRzo), and others that included the active observations  
823 available from two co-located RASS (one, RASS 915, associated with a 915-MHz, and the other,  
824 RASS 449, associated with a 449-MHz wind profiling radar). Radiosonde launches were used for  
825 verification of the retrieved profiles and Neural Network retrieved profiles were also used for  
826 comparison. ~~The NN retrievals used in this study were obtained either using the zenith angle  
827 only, or the average of the oblique scans (based on the averaged Tb of 15 and 165 degree  
828 scans) without including the zenith. Other MWR systems (Rose et al., 2005) provide retrieved  
829 profiles that include the information from both oblique and zenith scans. (see Appendix A).~~

**Formatted:** Outline numbered + Level: 1 + Numbering  
Style: 1, 2, 3, ... + Start at: 1 + Alignment: Left + Aligned  
at: 0.25" + Indent at: 0.5"

**Formatted:** Space After: 12 pt, Line spacing: Double,  
Border: Top: (No border), Bottom: (No border), Left: (No  
border), Right: (No border), Between : (No border)

830 Inclusion of the observations from the active RASS instruments in the PR approach  
831 improves the accuracy of the temperature profiles, particularly when ~~low-level~~ temperature  
832 inversions are present. Of the PRs configurations tested, we find better statistical agreement  
833 with the radiosonde observations when the RASS 449 is used together with the surface  
834 observations and brightness temperature from only the zenith MWR observations  
835 ~~(MWRz2sigma449)~~, and doubling the random radiometric uncertainty on the MWR  
836 observations (MWRz2sigma449) relative to the uncertainty calculated over the selected clear-  
837 sky days ~~(Fig. 1)~~. This configuration is also more accurate compared to MWRzo915 or  
838 MWRz2sigma915 (which use RASS 915 observation), because of the deeper RASS 449 height  
839 coverage. -The larger assumed radiometric uncertainty in the MWR Tb observations allows the  
840 retrieval to overcome both (a) the ~~{small}~~ systematic errors that exist between the MWR ~~(which~~  
841 ~~could be in either the~~ observed Tb values ~~or in the MonoRTM used as the forward model)~~ and  
842 the RASS, measurements and (b) the systematic errors that exist in forward microwave  
843 radiative models (Cimini et al. 2018).

844 We also selected 15 cases when temperature profiles from the radiosonde observations  
845 were the furthest from the mean climatological average, and reproduced the statistical  
846 comparison over this subset of cases. These are the cases usually the most difficult to retrieve  
847 and the most important to forecast; therefore, it is essential to improve the retrievals in these

848 situations. Even for this subset of selected cases we find that MWRz2sigma449 produces better  
849 statistics, proving that the inclusion of active sensor observations in MWR passive observations  
850 would be beneficial for improving the accuracy of the retrieved temperature profiles also in the  
851 upper layer of the atmosphere where RASS measurements are not available (at least up to 5 km  
852 AGL). However, we note that this result may be dependent on the fact that our oblique  
853 measurements were taken at a 15-degree elevation angle, and that MWRs in locations with  
854 unobstructed views allowing for scans down to 5 degrees may provide similar improvements to  
855 the temperature profile accuracy in the lowest 0-1 or even 0-2 km AGL layers (Crewell and  
856 Löhnert, 2007).

857 Finally, we also considered the impact of the inclusion of RASS measurements on the  
858 retrieved humidity profiles, but in this case the inclusion of RASS observations did not produce  
859 significantly better results, compared to the configurations that do not include them. This was  
860 not a surprise as RASS measures virtual temperature, effectively adding very little extra  
861 information to the water vapor retrievals. In this case a better option would be to consider  
862 adding other active remote sensors such as water vapor differential absorption lidars (DIALs) to  
863 the PRs. Turner and Löhnert (2020) showed that including the partial profile of water vapor  
864 observed by the DIAL substantially increases the information content in the combined water



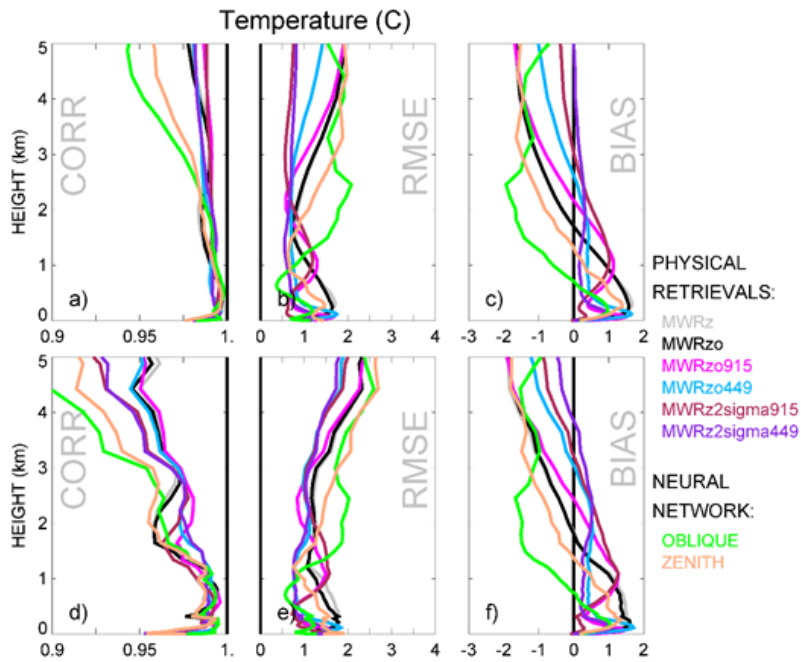
865 vapor retrievals. Consequently, to improve both temperature and humidity retrievals a synergy  
866 between MWR, RASS, and DIAL systems would likely be necessary.

867

868 **Appendix A**

869 The XPIA NN retrievals use a training dataset based on a 5-year climatology of profiles  
870 from radiosondes launched at the Denver International Airport, 35 miles south-east from the  
871 XPIA site. NN-based MWR vertical retrieval profiles were obtained using the zenith or an  
872 average of two oblique elevation scans, 15- and 165-degrees, all with 58 levels extending from  
873 the surface up to 10 km, with nominal vertical levels depending on the height (every 50 m from  
874 the surface to 500 m, every 100 m from 500 m to 2 km, and every 250 m from 2 to 10 km, AGL).

875 Fig. 1A shows composite NN vertical profiles of temperature (separately for the zenith  
876 and averaged obliques) calculated for radiosonde launch times, and the corresponding PR  
877 profiles already introduced in Fig. 6. As expected, the averaged oblique NN profile has lower  
878 bias and RMSE compared to the zenith NN profile below 1km AGL, while the zenith NN profile  
879 improved above this level.



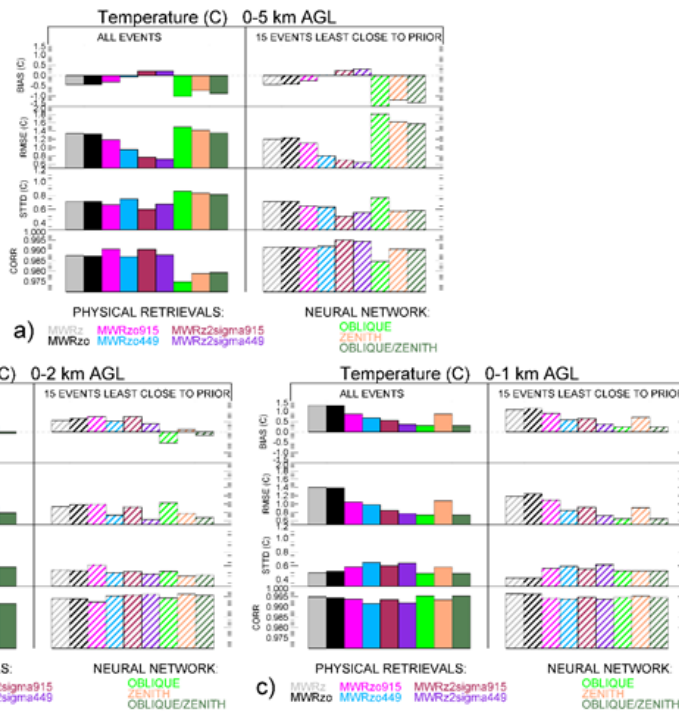
880  
 881 Fig. 1A. The same as Fig. 6 but with additional NN temperature profiles, from zenith in beige and  
 882 from averaged oblique – in green.

883  
 884 We note that in this comparison the MWR Tb data have been bias-corrected before  
 885 being used in the Physical Retrieval configurations, as discussed in Section 3.2, while the NN  
 886 retrievals use the uncorrected Tb, since it was non-trivial for us to reprocess those retrievals.  
 887 Zenith NN profiles have larger bias and RMSE and smaller correlation coefficient above 1 km

**Formatted:** Space After: 12 pt, Line spacing: Double,  
 Border: Top: (No border), Bottom: (No border), Left: (No  
 border), Right: (No border), Between : (No border)

888 AGL compared to all PR profiles. This is possibly due to the Tb bias in the transparent channels  
 889 of the V-band frequencies.

890 To optimize the use of the two types of NN scan data, we combined the NN retrieved  
 891 profiles using only the averaged oblique scans up to 1 km AGL and the zenith scans above 1 km.  
 892 Fig. 2A is the same as Fig. 8, now including also the three NN profiles (averaged oblique only,  
 893 zenith only, and their combination) presenting the statistics in three different layers of  
 894 atmosphere: from the surface to 5 km AGL, from the surface to 2 km AGL, and from the surface  
 895 to 1 km AGL (a, b and c panels).



896

**Formatted:** Space After: 12 pt, Line spacing: Double, Border: Top: (No border), Bottom: (No border), Left: (No border), Right: (No border), Between : (No border)

897 Fig. 2A. The same as Fig. 8 but including NN profile statistics from averaged oblique scans in  
898 beige, from zenith – in green, and from their combination – in spruce. Panels a, b, and c show  
899 the temperature statistics from the surface up to 5, 2 and 1 km AGL respectively.

900 Oblique only (and oblique and zenith combined) NN profiles show the best statistics in  
901 the layer closest to the surface, up to 1 km AGL, panel c, while in the deeper atmosphere layer  
902 up to 5 km all PR profiles have improved statistics compared to NNs, panel a. Panel b has mixed  
903 results: MWRz2sigma449 has the lowest RMSE, and the combined NN retrieved profiles show  
904 just slightly larger RMSE and almost the same standard deviation and correlation. It is  
905 important to admit that while potential NN bias-correction generally cannot change the oblique  
906 statistics, it may improve the zenith profiles, especially above 1 km AGL, therefore improving  
907 the combined NN profiles statistics.

#### 909 **Data availability**

910 All data are publicly accessible at the DOE Atmosphere to Electrons Data Archive and  
911 Portal, found at <https://a2e.energy.gov/projects/xpia> (Lundquist et al., 2016).

#### 913 **Author contribution**

914 Irina Djalalova completed the primary analysis with physical retrieval approach through  
915 MONORTM using XPIA data. Daniel Gottas contributed to the post-processing of the RASS data.

916 Irina Djalalova prepared the manuscript with contributions from all co-authors.

917

918 **Acknowledgements**

919 We thank all the people involved in XPIA for instrument deployment and maintenance,  
920 data collection, and data quality control, and particularly the University of Colorado Boulder for  
921 making the CU MWR data available. Funding for this study was provided by the NOAA/ESRL  
922 Atmospheric Science for Renewable Energy (ASRE) program.

923

924

925

926 **References**

927 Adachi, A. and H. Hashiguchi, 2019: Application of parametric speakers to radio acoustic  
928 sounding system. *Atmos. Meas. Tech.*, **12**, 5699–5715, 2019,  
929 <https://doi.org/10.5194/amt-12-5699-2019>.

930 Adler, B., J. M. Wilczak, L. Bianco, I. Djalalova, J. B. Duncan Jr., D. D. Turner, ~~2020~~2021:  
931 Observational case study of a persistent cold air pool and gap flow in the Columbia River  
932 Basin. *Under review to J. of Appl. In preparation Meteor. Climatol.*

933 Banta, R. M., and coauthors, 2020: Characterizing NWP model errors using Doppler lidar  
934 measurements of recurrent regional diurnal flows: Marine-air intrusions into the  
935 Columbia River Basin. *Month. Wea. Rev.*, **148**, 927-953, ~~doi:10.1175/MWR-D-19-~~  
936 ~~0188.1~~<https://doi.org/10.1175/MWR-D-19-0188.1>

Formatted: Indent: First line: 0"

Formatted: Border: Top: (No border), Bottom: (No border), Left: (No border), Right: (No border), Between : (No border)

Formatted: Space After: 12 pt, Line spacing: Double, Border: Top: (No border), Bottom: (No border), Left: (No border), Right: (No border), Between : (No border)

937 ~~Blumberg, W. G., D. D. Turner, S. M. Cavallo, J. Gao, J. Basara, A. Shapiro, 2019: An Analysis of~~  
938 ~~the Processes Affecting Rapid Near-Surface Water Vapor Increases during the Afternoon~~  
939 ~~to Evening Transition in Oklahoma. *J. of Appl. Meteorol. and Climatol.*, **58(10)**, 2217–~~  
940 ~~2234, <https://doi.org/10.1175/JAMC-D-19-0062.1>.~~

941 Bianco L., D. Cimini, F. S. Marzano, and R. Ware, 2005: Combining microwave radiometer and  
942 wind profiler radar measurements for high-resolution atmospheric humidity profiling, *J.*  
943 *Atmos. Ocean. Tech.*, **22**, 949–965, <https://doi.org/10.1175/JTECH1771.1>.

944 Bianco, L., K. Friedrich, J. M. Wilczak, D. Hazen, D. Wolfe, R. Delgado, S. Oncley, and J. K.  
945 Lundquist, 2017: Assessing the accuracy of microwave radiometers and radio acoustic  
946 sounding systems for wind energy applications. *Atmos. Meas. Tech.*, **10**, 1707-1721,  
947 <https://doi.org/10.5194/amt-10-1707-2017>.

948 Cadeddu, M. P., J. C. Liljegren, and D. D. Turner, 2013: The Atmospheric radiation measurement  
949 (ARM) program network of microwave radiometers: instrumentation, data, and  
950 retrievals, *Atmos. Meas. Tech.*, **6**, 2359–2372, [https://doi.org/10.5194/amt-6-2359-](https://doi.org/10.5194/amt-6-2359-2013)  
951 [2013](https://doi.org/10.5194/amt-6-2359-2013).

952 Cimini, D., ~~T. J. Hewison, L. Martin, J. Guldner, C. Gaffard, F. S. Marzano, 2006: Temperature and~~  
953 ~~humidity profile retrievals from ground-based microwave radiometers during TUC,~~  
954 ~~*Meteorologische Zeitschrift*, Vol. 15, No. 5, 45-56, DOI: 10.1127/09411-D-~~  
955 ~~2948/2006/0099~~

956 ~~Cimini, D., E. Campos, R. Ware, S. Albers, G. Giuliani, J. Oreamuno, P. Joe, S. E. Koch, S. Cober,~~  
957 ~~and E. Westwater, 2011: Thermodynamic Atmospheric Profiling during the 2010 Winter~~

958 [Olympics Using Ground-based Microwave Radiometry, \*IEEE Trans. Geosci. Remote Sens.\*,](#)  
959 [49, 12, <https://doi.org/10.1109/TGRS.2011.2154337>.](#)

960 [Cimini, D., Rosenkranz, P. W., Tretyakov, M. Y., Koshelev, M. A., and Romano, F., 2018:](#)  
961 [Uncertainty of atmospheric microwave absorption model: impact on ground-based](#)  
962 [radiometer simulations and retrievals, \*Atmos. Chem. Phys.\*, \*\*18\*\*, 15231–15259,](#)  
963 <https://acp.copernicus.org/articles/18/15231/2018/>.

964 [Cimini, D.,](#) M. Haeffelin, S. Kotthaus, U. Löhnert, P. Martinet, E. O'Connor, C. Walden, M.  
965 Collaud Coen, and J. Preissler, 2020: Towards the profiling of the atmospheric boundary  
966 layer at European scale—introducing the COST Action PROBE. *Bulletin of Atmospheric*  
967 *Science and Technology*, **1**, 23–42, <https://doi.org/10.1007/s42865-020-00003-8>.

968 ~~Cimini, D., Rosenkranz, P. W., Tretyakov, M. Y., Koshelev, M. A., and Romano, F., 2018:~~  
969 ~~Uncertainty of atmospheric microwave absorption model: impact on ground-based~~  
970 ~~radiometer simulations and retrievals, *Atmos. Chem. Phys.*, **18**, 15231–15259,~~  
971 ~~<https://acp.copernicus.org/articles/18/15231/2018/>.~~

972 Clough, S.A., M. W. Shephard, E. J. Mlawer, J. S. Delamere, M. Iacono, K. E. Cady-Pereira, S.  
973 Boukabara and P. D. Brown, [2005](#): Atmospheric radiative transfer modeling: A summary  
974 of the AER codes, *JQSRT*, vol 91, no. 2, pp 233-244, [2005](#),  
975 <https://doi.org/10.1016/j.jqsrt.2004.05.058>.

976 [Crewell, S., U. Löhnert, 2007: Accuracy of Boundary Layer Temperature Profiles Retrieved With](#)  
977 [Multifrequency Multiangle Microwave Radiometry, \*IEEE TGRS\*, VOL. 45, NO. 7, JULY](#)  
978 [2007, DOI: 10.1109/TGRS.2006.888434.](#)

**Formatted:** Font color: Custom Color(17,85,204)

**Formatted:** Space After: 12 pt, Line spacing: Double,  
Border: Top: (No border), Bottom: (No border), Left: (No  
border), Right: (No border), Between : (No border)

979 Engelbart, D., W. Monna, J. Nash, 2009: Integrated Ground-Based Remote-Sensing Stations for  
980 Atmospheric Profiling, *COST Action 720 Final Report*, EUR 24172,  
981 <https://doi.org/10.2831/10752>.

982 Görsdorf, U., and V. Lehmann, 2000: Enhanced Accuracy of RASS-Measured Temperatures Due  
983 to an Improved Range Correction. *J. Atmos. Oceanic Technol.*, **17** (4), 406–416,  
984 [https://doi.org/10.1175/1520-0426\(2000\)017<0406:EAORMT>2.0.CO;2](https://doi.org/10.1175/1520-0426(2000)017<0406:EAORMT>2.0.CO;2).

985 Han, Y., and E. R. Westwater, 1995: Remote sensing of tropospheric water vapor and cloud  
986 liquid water by integrated ground-based sensors. *J. Atmos. Oceanic Tech.*, **12**, 1050-  
987 1059, DOI: [https://doi.org/10.1175/1520-0426\(1995\)012<1050:RSOTWV>2.0.CO;2](https://doi.org/10.1175/1520-0426(1995)012<1050:RSOTWV>2.0.CO;2)

988 ~~Han, Y., Hewison, T., 2007: 1D-VAR Retrieval of Temperature and E. R. Westwater, 2000:~~  
989 ~~Analysis and improvement of tipping calibration for ground-based microwave~~  
990 ~~radiometers. Humidity Profiles From a Ground-Based Microwave Radiometer, IEEE~~  
991 ~~Trans. Geosci. Remote Sens., **38**, 1260–1276, **45**(7), 2163–2168,~~  
992 ~~<https://doi.org/10.1109/TGRS.2007.898091>.~~  
993 ~~<https://doi.org/10.1109/36.843018>.~~

994 Horst, T. W., S. R. Semmer, and I. Bogoev, 2016: Evaluation of Mechanically-Aspirated  
995 Temperature/Relative Humidity Radiation Shields, *18th Symposium on Meteorological*  
996 *Observation and Instrumentation, AMS Annual Meeting*, New Orleans, LA, 10-15 January  
997 2016, <https://ams.confex.com/ams/96Annual/webprogram/Paper286839.html>.

998 Kaimal, J. C., and J. E. Gaynor, 1983: The Boulder Atmospheric Observatory. *J. Climate Appl.*  
999 *Meteor.*, **22**, 863–880, [https://doi.org/10.1175/1520-](https://doi.org/10.1175/1520-0450(1983)022<0863:TBAO>2.0.CO;2)  
1000 [0450\(1983\)022<0863:TBAO>2.0.CO;2](https://doi.org/10.1175/1520-0450(1983)022<0863:TBAO>2.0.CO;2).



1001 Küchler, N., D. D. Turner, U. Löhnert, and S. Crewell, 2016: Calibrating ground-based microwave  
1002 radiometers: Uncertainty and drifts, *Radio Sci.*, **51**, 311–  
1003 327, [doi:10.1002/2015RS005826](https://doi.org/10.1002/2015RS005826).

1004 Löhnert U. and O. Maier, 2012: Operational profiling of temperature using ground-based  
1005 microwave radiometry at Payerne: prospects and challenges. *Atmos. Meas. Tech.*, **5**,  
1006 1121–1134, <https://doi.org/10.5194/amt-5-1121-2012>.

1007 Lundquist, J. K., J. M. Wilczak, R. Ashton, L. Bianco, W. A. Brewer, A. Choukulkar, A. Clifton, M.  
1008 Debnath, R. Delgado, K. Friedrich, S. Gunter, A. Hamidi, G. V. Iungo, A. Kaushik, B.  
1009 Kosović, P. Langan, A. Lass, E. Lavin, J. C.-Y. Lee, K. L. McCaffrey, R. K. Newsom, D. C.  
1010 Noone, S. P. Oncley, P. T. Quelet, S. P. Sandberg, J. L. Schroeder, W. J. Shaw, L. Sparling,  
1011 C. St. Martin, A. St. Pe, E. Strobach, K. Tay, B. J. Vanderwende, A. Weickmann, D. Wolfe,  
1012 and R. Worsnop, 2017: Assessing state-of-the-art capabilities for probing the  
1013 atmospheric boundary layer: the XPIA field campaign. *Bull. Am. Meteor. Soc.*, **98**, 289–  
1014 314, <https://doi.org/10.1175/BAMS-D-15-00151.1>.

1015 Maahn, M., D. D. Turner, U. Löhnert, D. J. Posselt, K. Ebell, G. G. Mace, and J. M. Comstock,  
1016 2020: Optimal estimation retrievals and their uncertainties: What every atmospheric  
1017 scientist should know. *Bull. Amer. Meteor. Soc.*, **101**, E1512-E1523,  
1018 <https://doi.org/10.1175/BAMS-D-19-0027.1>

1019 ~~May P. T., Moran, K. P., and Strauch, R. G., 1989: The Accuracy of RASS Temperature~~  
1020 ~~Measurements, *J. Appl. Meteorol.*, **28**, 1329–1335.~~

- 1021 Maddy, E. S. and C. D. Barnet, 2008: Vertical Resolution Estimates in Version 5 of AIRS  
1022 Operational Retrievals. *IEEE TGRS*, VOL. 46, NO. 8, AUGUST 2008,  
1023 <https://doi.org/10.1109/TGRS.2008.917498>
- 1024 Martinet, P., D. Cimini, F. Burnet, B. Ménétrier, Y. Michel, and V. Unger, 2020: Improvement of  
1025 numerical weather prediction model analysis during fog conditions through the  
1026 assimilation of ground-based microwave radiometer observations: a 1D-Var study,  
1027 *Atmos. Meas. Tech.*, **13**, 6593–6611, <https://doi.org/10.5194/amt-13-6593-2020>.
- 1028 May, P. T. and J. M. Wilczak, 1993: Diurnal and Seasonal Variations of Boundary-Layer Structure  
1029 Observed with a Radar Wind Profiler and RASS. *Mon. Wea. Rev.*, **121**, 673–682,  
1030 [https://doi.org/10.1175/1520-0493\(1993\)121<0673:DASVOB>2.0.CO;2](https://doi.org/10.1175/1520-0493(1993)121<0673:DASVOB>2.0.CO;2).
- 1031 Masiello, G., C. Serio, and P. Antonelli, 2012: Inversion for atmospheric thermodynamical  
1032 parameters of IASI data in the principal components space. *Quart. J. Roy. Meteor. Soc.*,  
1033 **138**, 103–117, <https://doi.org/10.1002/qj.909>.
- 1034 Merrelli, A. M., and D. D. Turner, 2012: Comparing information content of upwelling far infrared  
1035 and midinfrared radiance spectra for clear atmosphere profiling. *J. Atmos. Oceanic*  
1036 *Technol.*, **29**, 510–526, <https://doi.org/10.1175/JTECH-D-11-00113.1>.
- 1037 Neiman, P. J., D. J. Gottas, and A. B. White, 2019: A Two-Cool-Season Wind Profiler–Based  
1038 Analysis of Westward-Directed Gap Flow through the Columbia River Gorge. *Month.*  
1039 *Wea. Rev.*, **147**, 4653–4680, <https://doi.org/10.1175/MWR-D-19-0026.1>.
- 1040 North, E. M., A. M. Peterson, and H. D. Parry, 1973: RASS, a remote sensing system for  
1041 measuring low-level temperature profiles. *Bull. Am. Meteor. Soc.*, **54**, 912–919.

1042 Payne, V. H., J. S. Delamere, K. E. Cady-Pereira, R. R. Gamache, J.-L. Moncet, E. J. Mlawer, and S.  
1043 A. Clough, 2008: Air-broadened half-widths of the 22- and 183-GHz water-vapor lines.  
1044 *IEEE Trans. Geosci. Remote Sens.*, **46**, 3601-3617,  
1045 [doi:10.1109/TGRS.2008.2002435](https://doi.org/10.1109/TGRS.2008.2002435).  
1046 Payne, V. H., E. J. Mlawer, K. E. Cady-Pereira, and J.-L. Moncet, 2011: Water vapor continuum  
1047 absorption in the microwave. *IEEE Trans. Geosci. Remote Sens.*, **49**, 2194-2208,  
1048 [doi:10.1109/TGRS.2010.2091416](https://doi.org/10.1109/TGRS.2010.2091416).  
1049 Rodgers, C. D., 2000: Inverse Methods for Atmospheric Sounding: Theory and Practice. *Series on*  
1050 *Atmospheric, Oceanic and Planetary Physics*, Vol. 2, World Scientific, 238 pp.  
1051 ~~Rose, T., S. Crewell, U. Löhnert, C. Simmer, 2005: A network suitable microwave radiometer for~~  
1052 ~~operational monitoring of the cloudy atmosphere, *Atmospheric Research*, **75**, Issue 3,~~  
1053 ~~183–200, <https://doi.org/10.1016/j.atmosres.2004.12.005>.~~  
1054 Rosenkranz, P. W., 1998: Water vapour microwave continuum absorption: A comparison of  
1055 measurements and models. *Radio Science*, **33**, 919–928,  
1056 <https://doi.org/10.1029/98RS01182>.  
1057 Shaw, W., and Coauthors, 2019: The Second Wind Forecast Improvement Project (WFIP 2):  
1058 General Overview. *Bull. Am. Meteor. Soc.*, **100(9)**, 1687–1699,  
1059 <https://doi.org/10.1175/BAMS-D-18-0036.1>.

**Formatted:** Space After: 12 pt, Border: Top: (No border),  
Bottom: (No border), Left: (No border), Right: (No  
border), Between : (No border)

**Formatted:** Space After: 12 pt, Line spacing: Double,  
Border: Top: (No border), Bottom: (No border), Left: (No  
border), Right: (No border), Between : (No border)

- 1060 Solheim, F., J. R. Godwin, J., and R. Ware, 1998a: Passive ground-based remote sensing of  
1061 atmospheric temperature, water vapor, and cloud liquid profiles by a frequency  
1062 synthesized microwave radiometer. *Meteorol. Z.*, **7**, 370–376.
- 1063 Solheim F., J. R. Godwin, E. R. Westwater, Y. Han, S. J. Keihm, K. Marsh, R. Ware, 1998b:  
1064 Radiometric profiling of temperature, water vapor and cloud liquid water using various  
1065 inversion methods. *Radio Science*, **33**, 393–404, <https://doi.org/10.1029/97RS03656>.
- 1066 Stankov, B. B., E. R. Westwater, and E. E. Gossard, 1996: Use of wind profiler estimates of  
1067 significant moisture gradients to improve humidity profile retrieval. *J. Atmos. Oceanic  
1068 Tech.*, **13**, 1285–1290-, DOI: [https://doi.org/10.1175/1520-  
1069 0426\(1996\)013<1285:UOWPEO>2.0.CO;2](https://doi.org/10.1175/1520-0426(1996)013<1285:UOWPEO>2.0.CO;2).
- 1070 Strauch, R. G. , D. A. Merritt, K. P. Moran, K. B. Earnshaw, and D. V. De Kamp, 1983: The  
1071 Colorado wind-profiling network. *J. Atmos. Oceanic Technol.*, **1**, 37–49,  
1072 [https://doi.org/10.1175/1520-0426\(1984\)001<0037:tcwpm>2.0.co;2](https://doi.org/10.1175/1520-0426(1984)001<0037:tcwpm>2.0.co;2).
- 1073 Turner, D. D., and U. Löhnert, 2014: Information content and uncertainties in thermodynamic  
1074 profiles and liquid cloud properties retrieved from the ground-based Atmospheric  
1075 Emitted Radiance Interferometer (AERI). *J. Appl. Meteor. Clim.*, **53**, 752–771,  
1076 <https://doi.org/10.1175/JAMC-D-13-0126.1>.
- 1077 Turner, D. D., and W. G. Blumberg, 2019: Improvements to the AERIOe thermodynamic profile  
1078 retrieval algorithm. *IEEE Journal of Selected Topics in Applied Earth Observations and  
1079 Remote Sensing*, **12(5)**, 1339–1354, <https://doi.org/10.1109/JSTARS.2018.2874968>.

1080 Turner, D. D., and U. Löhnert, 2020: Ground-based Temperature and Humidity Profiling:  
1081 Combining Active and Passive Remote Sensors. *In revision to Atmos. Meas. Tech.*  
1082 ~~Discuss., <https://doi.org/10.5194/amt-2020-352>~~Discuss., [https://doi.org/10.5194/amt-](https://doi.org/10.5194/amt-2020-352)  
1083 [2020-352](https://doi.org/10.5194/amt-2020-352).

1084 Ware R., Solheim F., Carpenter R., and Coauthors, 2003: A multi-channel radiometric profiler of  
1085 temperature, humidity and cloud liquid. *Radio Science*, **38**, No. 4, 8079,  
1086 <https://doi.org/10.1029/2002RS002856>.

1087 Weber, B. L., D. B. Wuertz, D. C. Welsh, and R. Mcpeek, ~~1992~~1993: Quality controls for profiler  
1088 measurements of winds and RASS temperatures. *J. Atmos. Oceanic Technol.*, **10**, 452–  
1089 464, [https://doi.org/10.1175/1520-0426\(1993\)010<0452:gcfpmo>2.0.co;2](https://doi.org/10.1175/1520-0426(1993)010<0452:gcfpmo>2.0.co;2)

1090 Wilczak, J. M., and Coauthors, 2019: The Second Wind Forecast Improvement Project (WFIP2):  
1091 Observational Field Campaign. *Bull. Am. Meteor. Soc.*, **100(9)**, 1701–1723,  
1092 <https://doi.org/10.1175/BAMS-D-18-0035.1>.

1093 Wolfe, D. E. and R. J. Latatits, 2018: Boulder Atmospheric Observatory: 1977–2016: The end of  
1094 an era and lessons learned. *Bull. Am. Meteor. Soc.*, **99**, 1345–1358,  
1095 <https://doi.org/10.1175/BAMS-D-17-0054.1>.